Escola Tècnica Superior d'Enginyeries

Departament de Ciències de la Computació

Automatic adventitia segmentation in IntraVascular UltraSound images

Memòria del Treball Experimental presentat per **Aura Hernàndez i Sabaté** i dirigit per **Debora Gil Resina i Petia Ivanova Radeva** dins del Programa de Doctorat en Informàtica, opció **Visió per Computador**, de la Universitat Autònoma de Barcelona.

les Dres. Debora Gil Resina i Petia Ivanova Radeva, del Departament de Ciències de la Computació de la Universitat Autònoma de Barcelona,

CERTIFIQUEN

que la present memòria ha estat realitzada sota la seva direcció per n' **Aura Hernàndez i Sabaté** i constitueix el Treball Experimental del *Programa de Tercer Cicle d'Informàtica, opció Visió per Computador*.

Bellaterra, Setembre, 2005

Debora Gil Resina i Petia Ivanova Radeva

AGRAÏMENTS

No hauria arribat fins on sóc sense l'incondicional suport del Lluís, qui un dia va apostar per mi i més tard va accedir a tenir un sou decent per tal que jo pogués iniciar aquesta carrera renunciant ell a iniciar-la. Aquell dia vaig anar a parar al CVC, on la Petia va dipositar la seva confiança en mi el mateix dia que em va conèixer. Més endavant, vaig conèixer a la que seria la meva segona jefa, la Debora, qui, entre riures, bronques i cigarros m'ha ensenyat moltes de les coses que he après durant tot aquest temps. Tampoc seria aquí si no hagués estat per l'ambient que he respirat aquests dos anys, per tots aquests esmorzars i dinars en els que intentem arreglar el món o, si més no, passar una bona estona rient.

Però per arribar a estar entre aquestes quatre parets, ha estat essencial el suport dels meus pares, Jeroni i Núria, que han estat al meu costat en tot moment i m'han demostrat que les coses es fan amb força de voluntat, rebeldia, persistència i, sobretot, amb ganes de fer-les.

També he tingut el suport del meu considerat fill adoptiu Gerard que, amb els seus comentaris he rigut i he oblidat els mals moments. I parlant de mals moments, vull donar les gràcies a tots aquells que, d'una manera o altra, heu estat al meu costat en el pitjor moment. No cal dir noms, perquè segur que me n'oblido algun, així que gràcies!

RESUM

Una tècnica molt útil en el diagnòstic de les malalties coronàries és la caracterització de les diferents plaques mitjançant l'anàlisi de seqüències d'Ecografia Intracoronària. La detecció manual de les vores lumen-íntima, íntima-mitjana i mitjana-adventícia constitueix una gran part de l'activitat dels experts per al procés de la quantificació de la placa. La gran varietat de descriptors de les vores del vas, a més de les ombres, artefactes i la resposta difusa deguda a les propietats físiques de l'ultrasò, dificulta la segmentació automàtica de la vora mitjana-adventícia. Aquest treball experimental presenta una solució a aquest problema tan complex. El procediment es basa en la unió de l'ús d'operadors avançats de filtratge anisotròpic amb tècniques de classificació estadística, assolint una estratègia eficient per al modelatge dels vasos coronaris. Inicialment es fa una introducció a la base teòrica de què consta el mètode. Tot seguit s'introdueixen els passos de l'algorisme, per acabar validant el mètode amb estadístiques que demostren que la detecció de la vora mitjana-adventícia s'assoleix amb una precisió dins de la variabilitat inter-observador, malgrat la naturalesa de la placa, la geometria del vas i les vores incompletes d'alguns. Finalment, es presenta una petita aplicació en Matlab per a la segmentació automàtica de la vora mitjana-adventícia.

Paraules clau: *Ecografia Intracoronària, adventícia, segmentació automàtica, classificació, processament anisotròpic*

ABSTRACT

A usual tool in cardiac disease diagnosis is vessel plaque assessment by analysis of IVUS sequences. Manual detection of lumen-intima, intima-media and media-adventitia vessel borders is the main activity of physicians in the process of plaque quantification. Large variety in vessel border descriptors, as well as, shades, artifacts and blurred response due to ultrasound physical properties troubles automated media-adventitia segmentation. This experimental work presents a solution to such a complex problem. The process blends advanced anisotropic filtering operators and statistic classification techniques, achieving an efficient vessel border modelling strategy. First of all, we introduce the theoretic base of the method. After that, we show the steps of the algorithm, validating the method with statistics that show that the media-adventitia border detection achieves an accuracy in the range of inter-observer variability regardless of plaque nature, vessel geometry and incomplete vessel borders. Finally, we present a little Matlab application to the automatic media-adventitia border.

Keywords: *IntraVascular UltraSound, adventitia, automatic segmentation, classification, anisotropic processing*

Contents

List of Figures

Chapter 1

Introduction

1.1 The Clinical Problem

Cardiovascular disease (heart, stroke and blood vessel disease) is a leading cause of death in developed countries. While the heart pumps blood, the muscle gets its nutrition from the pumped blood coming back into the muscle via the coronary arteries, so coronary artery disfunction is a strong point in cardiovascular disease treatments. Artery problems develop over time when plaque (a combination of blood cholesterol, fat and cells) builds up on the inside walls of arteries. Plaque makes arteries less flexible (atherosclerosis) and narrows the artery's blood flow (stenosis).

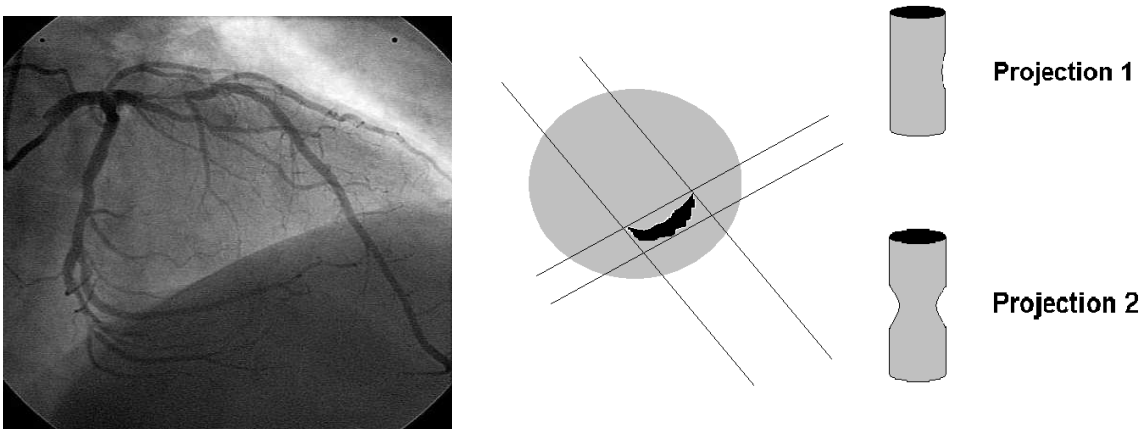

(a) (b)

Figure 1.1: Coronary Angiography diagnosis. Angiographic plane (a) and stenosis diagnosis(b).

Coronary angiography (fig. 1.1(a)) is one of the most used method for making a diagnosis of coronary artery disease, though it is also the most invasive. It is a form of cardiac catheterization that shows the heart's chambers, great vessels, and coronary arteries using x-ray technology. A contrast dye is injected to make the heart and vessels visible on x-ray cinematography. Angiography images show a spatial vision of coronary tree making possible the evaluation of vessel geometry. However, there is a lack of information about vessel morphology and assessment of plaque narrowing in the perpendicular direction to the angiographic plane might be underestimated. This artifact is intrinsic to the projection nature

of angiographies acquisition, which only produces a projection of the coronary tree. It follows that the stenosis visualization depends on the projection direction (as we show in figure 1.1(b)). If the stenosis is not on the projection direction, it is visible (projection 2 in fig.1.1(b)), whereas if it is in the same direction, it keeps hidden (projection 1 in fig.1.1(b)).

To overcome angiography's limitations, IntraVascular UltraSound (IVUS) was developed towards the end of the 1980s and has been refined and its clinical importance assessed through the 1990s. Intravascular ultrasound is an invasive procedure, performed along main arteries with cardiac catheterization. A transducer is threaded through the coronary arteries and, using high-frequency sound waves, produces detailed images of the interior walls of the arteries. IVUS imaging is a useful clinical tool [1] that provides cardiologists with a cross sectional view of the vessel (fig.1.2) and allows a complete study of its morphology, such as arterial wall, lumen or plaque.

1.1.1 IntraVascular UltraSound

In coronary arteries there are frequently three layers [2]. The innermost layer consists of a complex of three elements: intima, atheroma (in diseased arteries), and internal elastic membrane. The trailing edge of the intima cannot always be distinguished clearly. Moving outward from the lumen, the second layer is the media, which is usually less echogenic than the intima. In some cases the media may appear artifactually thin because of an intense reflection from the intima or external elastic membrane (EEM). The third and outer layer consists of the adventitia and periadventitial tissues. There is no distinct boundary on IVUS images separating the true adventitia from surrounding perivascular tissues. Depending on the disease of the artery, different kind of plaques can be distinguished: calcified, soft and fibrous and mixed plaque. The main advantage of IVUS sequences over angiography imaging is that most of the plaques visible in IVUS images do not appear in angiography images. In fact, it has been determined that in a coronary stenosis quantification by Ultrasound, those areas considered normals by angiography are affected with a mean luminal area reduction of 40% [3].

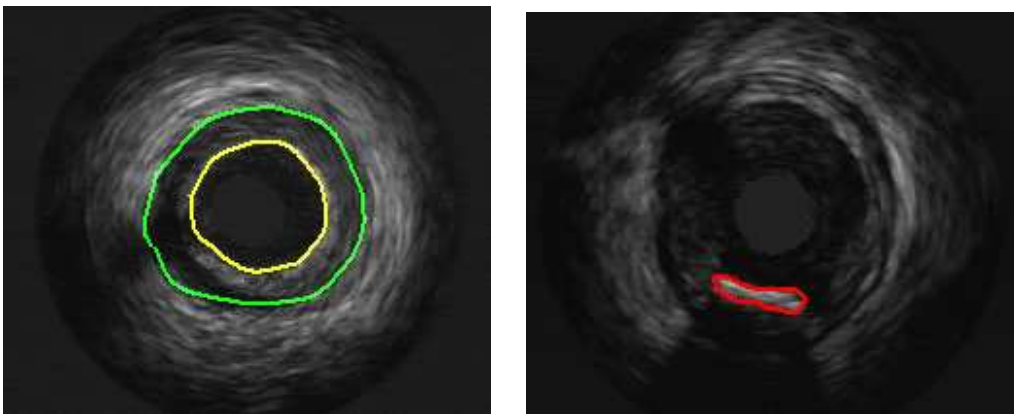

(a) (b)

Figure 1.2: Vessel Borders (a) and Calcium (b) Identification. Intima in yellow, adventitia in green and calcium in red.

The technique helps diagnosis and treatment of cardiac diseases, as far as a precise characterization and segmentation of arterial structures is available. In order to achieve a good diagnosis and so, an appropriate treatment, different measures relative to lumen, stenosis, atheroma, EEM and calcium and

different plaques are essential. Lumen measurements are performed using the interface between the lumen and the leading edge of the intima (yellow in fig.1.2(a)). On the other hand, a discrete interface at the border between the media and the adventitia is almost invariably present within IVUS images and corresponds closely to the location of the EEM (green in fig.1.2(a)). It follows that it is necessary to segment these borders to achieve reliable measurements, as well as, an exhaustive characterization of all kind of plaques. For convenience, we will talk about either lumen or intima segmentation to refer to the segmentation of the inner border and adventitia to refer to the outer border. In the case of calcium (red in fig.1.2(b)), there is an acoustic shadowing behind them, because calcium provides a complete reflection of the signal. It follows that adventitia is performed by extrapolation from the closest identifiable EEM border. A manual processing of images for the target structures characterization, apart from being a tedious time consuming task, might suffer from intra- and inter- observer variability. This fact motivates the development of image processing techniques addressing detection of arterial structures.

1.2 Classic Segmentation Approaches

Since the early years, many algorithms for a reliable intima detection have been proposed ([4]-[12]). By its inherent difficulty (its distance from the transducer reduces sharpness in the border visual appearance), adventitia modelling has been only approached in recent works ([13]-[22]). Nevertheless, an accurate border detection requires either elaborated strategies in the case of contour based segmentations ([18]-[22]), or a previous plaque and tissue characterization in the case of classification strategies ([15], [16]).

Usual techniques addressing segmentation of vessel borders (intima and adventitia) rely on a single local image descriptor (usually edges) to guide a snake towards the target structures ([4]-[7], [15]-[22]). Regardless of low quality in IVUS images, adventitia detection adds the difficulty of a large variety of descriptors, a weak visual appearance by a decrease in the ultrasonic pulse energy [25] and incomplete contours due to echo opaque plaques (e.g. calcium) shadowing. It follows that standard segmentation approaches do not suffice by their own and need exclusive strategies to yield proper results. Some authors [4]-[6], [21], [22] combine transversal and longitudinal contours to endow the model with spatial continuity along the sequence. In this case, the use of ECG-gated sequences [6], [7], [15] significantly helps to achieve a reliable segmentation of longitudinal cuts. Other approaches ([8], [11], [15]) manually restrict a region of interest that serves to initialize a snake, although such initialization might need to be updated along the sequence.

A common inconvenience of segmentations based on contour detection is that they require some kind of image filtering to avoid fake responses. The poor image quality as well as large variety of IVUS artifacts (calcium, side-branches, shadows, catheter guide and blood back scatter) make standard anisotropic smoothings [41] fail to achieve optimal results. In order to overcome these drawbacks, several approaches have been proposed. The most simple strategy is to discard those images containing too much artifacts [18]. Although this is a practical way of filtering, it runs the risk of losing too much information for a reliable recovery of vessel borders. Others ([12],[24]), directly handle raw data (the ultrasound signal before being digitalized) and filter impulse responses of the transducer. Unfortunately, raw data acquisition needs of a special device not always available in standard clinical equipments.

Recent approaches ([12]-[17], [26]) use classification strategies to better characterize coronary structures (plaque and vessel borders). Although results are robust to noise and artifacts, most of them ([12],

[15], [16]) require plaque classification to yield, as a side result, lumen and media-adventitia segmentation. The only statistical proposal that directly handles vessel borders detection is discriminant snakes [26], which extract the *a priori* knowledge for the segmentation of the current frame from the previous segmented image. Although they are well suited for border tracking (thus avoiding any interaction along the sequence), they require an accurate segmentation of the first sequence frame for each different case.

We argue that vessel borders detection should serve to characterize and quantify vessel plaque rather than follow as a side result of a laborious plaque classification. In the present work, we describe a plaque classification free method for adventitia detection based on a statistical extraction of adventitia points followed by the recovery of a closed model determined by the image geometry.

1.3 Our Contribution

An analysis of the limitations and advantages of each of the previously reported approaches suggests that a robust adventitia segmentation should combine classification strategies with advanced filtering and segmentation techniques [32]. The deterministic-statistical strategy for adventitia detection we propose is a three-fold algorithm: preprocessing of IVUS images, selection of points on the vessel border and segmentation of the extracted points. In the preprocessing step, a restricted anisotropic diffusion [33] sharpens vessel borders appearance in the polar transform of each IVUS frame. Supervised classification techniques serve to compute 2 binary images: one for calcium sectors and another one for vessel borders. The first image is a mask that discards sectors of ambiguous information. The second one is a collection of fragmented vessel segments that are modelled by computing an implicit closed representation and, then, an explicit B-spline parameterization. An anisotropic contour closing [34] yields the implicit closed model of vessel segments conforming to the Gestalt principles of good continuation and avoiding interpolation at calcium and side-branches sectors. Parametric B-spline snake with the initial snake at the outer radius are used to compute the final explicit compact model.

The present work is structured as follows. In chapters 2 and 3 we introduce the basis of the tools we use, either statistical (chapter 2) or deterministic (chapter 3). The thoroughly explanation of the algorithm is detailed in chapter 4. The extended chapter 5 is dedicated to present the validation of the method, showing real cases (5.3) and their statistical results (5.3.1). In chapter 6 we present a prototype application for the use of the clinical experts in the Hospital Universitari Germans Trias i Pujol in Badalona (Spain). Finally, in chapter 7, we discuss from the failed cases the drawbacks of the strategy and conclude with the ideas for the future work.

Chapter 2

Statistical Tools

Statistical procedures are those that, rather than yielding a unique output value, weight a wide range of outcomes with their probability of being realized. In computer vision, a main use of statistics is object classification and pattern recognition based on the mechanisms of human vision. Human vision produces, from external images, a description of target objects that discards irrelevant information, and allows the observer processing visual data and distinguishing the different objects in the scene. In a classification framework, the former physiological steps turn into three main operations:

1. **Feature extraction**. As human vision does, it consists in extracting those descriptors that best characterize the different target objects in an image. The collection of all descriptors produces, for each pixel j, an n-dimensional feature vector, $Y_j = (y_1, y_2, \ldots, y_n)$. The real n-dimensional space representing these vectors is called the feature space.

2. **Dimensionality reduction** can be applied depending on the dimensions of the feature space to reduce high dimensionality and discard irrelevant and/or redundant information.

3. **Classification** is concerned about visual information processing. There are two different strategies for object discrimination: unsupervised and supervised techniques. In unsupervised approaches the system clusters the input objects by similarity in their descriptors without any explicit supervision. Supervised strategies divide the process in two stages: a learning stage to recognize the different objects and label them as classes, dividing the resulting feature space and a test stage to identify a new attribute by means of the trained classes.

2.1 Image Feature Descriptors

A delicate main step in a classification procedure is to choose the features that represent our data. The goal is to produce an appropriate set of characteristics that allows discriminating the different objects to classify. For instance, if we want to describe a human face, it is enough to use characteristics such as two eyes, one nose and one mouth, but these features are not enough to distinguish its gender.

Image gray value descriptors can be split into two main classes: gray level discontinuity measures and gray values statistics. The first class are local descriptors which are concerned with gray values local changes. The second group might be regarded as global descriptors since they provide information about the distribution of image gray values.

1. Local variability Descriptors. Local descriptors are those that, for each pixel, take into account only a small neighborhood of the image pixel. Usually they are discontinuity operators in the sense that they quantify abrupt changes in image gray values. In the context of computer vision, this corresponds to oriented edge and crease (ridges and valleys) detection. Because it emulates the mechanisms of our visual system, the standard way of determining such discontinuities is by convolving the image with the directional derivatives of an anisotropic Gaussian kernel.

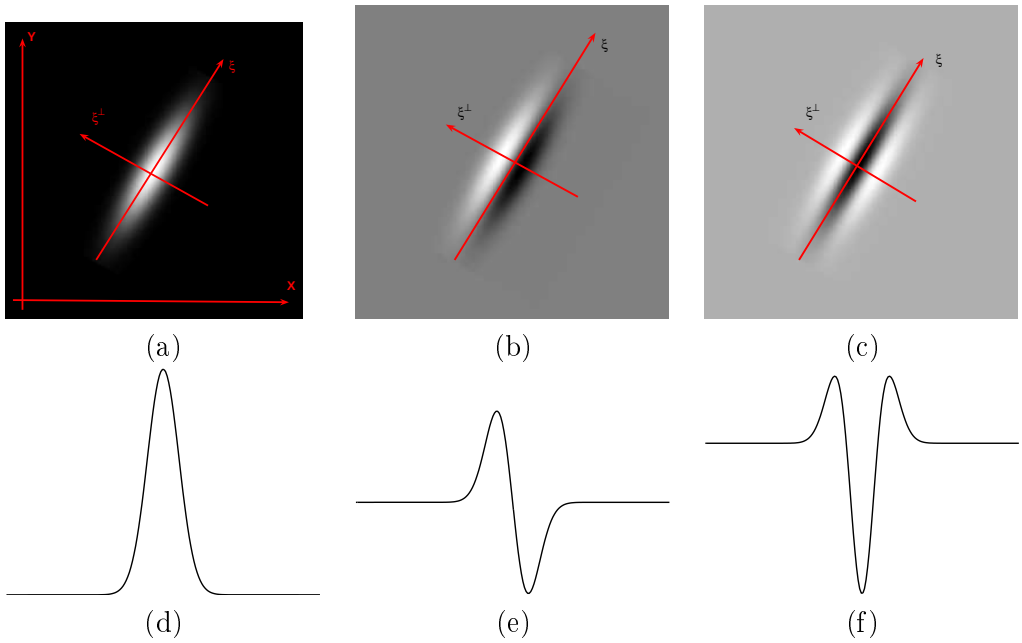

Figure 2.1: Oriented Gaussian derivatives. Oriented Gaussian (a) first derivative (b) and second (c). Projections on ξ direction of the oriented Gaussian (d), first (e) and second derivative (f).

Let $\tilde{X} = \xi$, $\tilde{Y} = \xi^{\perp}$ be the oriented axis given by

$$\begin{pmatrix} \tilde{X} \\ \tilde{Y} \end{pmatrix} = \begin{pmatrix} \xi \\ \xi^{\perp} \end{pmatrix} = \begin{pmatrix} cos(\theta) & -sin(\theta) \\ sin(\theta) & cos(\theta) \end{pmatrix} \begin{pmatrix} X \\ Y \end{pmatrix}$$

If G is an anisotropic Gaussian kernel oriented in axes $\tilde{X}, \tilde{Y}$, of mean 0 and standard deviations (σ_1, σ_2):

$$G = \frac{1}{2\pi\sqrt{\sigma_1\sigma_2}} e^{-\frac{1}{2}\left[\frac{\tilde{x}^2}{\sigma_1^2}+\frac{\tilde{y}^2}{\sigma_2^2}\right]}$$

its first and second derivatives are the following 2-dimensional kernels:

$$G_{\tilde{y}} = -\frac{\tilde{y}}{\sigma_2^2 2\pi\sqrt{\sigma_1\sigma_2}} e^{-\frac{1}{2}\left[\frac{\tilde{x}^2}{\sigma_1^2}+\frac{\tilde{y}^2}{\sigma_2^2}\right]} \qquad G_{\tilde{y}\tilde{y}} = \frac{\tilde{y}^2 - \sigma_2^2}{\sigma_2^4 2\pi\sqrt{\sigma_1\sigma_2}} e^{-\frac{1}{2}\left[\frac{\tilde{x}^2}{\sigma_1^2}+\frac{\tilde{y}^2}{\sigma_2^2}\right]}$$

which yield oriented derivatives of an image I by convolving:

$$G_{\tilde{y}} * I = \langle \nabla \tilde{I}, \tilde{y} \rangle = D_{\tilde{y}} \tilde{I}$$

where $\tilde{I}$ is the convolution of I with G, $\tilde{I} = G * I$. Figure 2.1 shows the convolving kernels of a

oriented Gaussian (a), and its first (b), and second (c) derivatives along the $\xi^{\perp}$ direction as well as their respective projections (d), (f), (g) on the ξ direction.

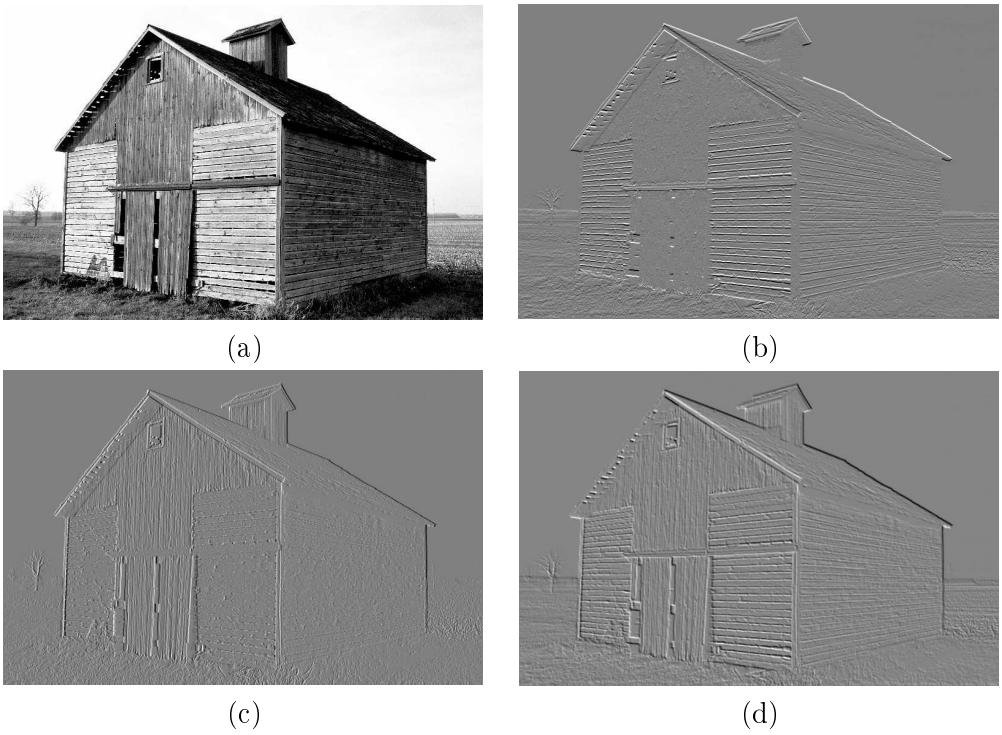

Figure 2.2: Local Descriptors 1. First derivatives as discontinuity measures, for the computation of directional edges.

Figures 2.2 and 2.3 show filters for edges (fig.2.2) and ridges (fig.2.3) detections. Original images are shown in fig.2.2(a), fig.2.3(a). As we can observe, in fig.2.2(b), horizontal edges are enhanced while vertical ones are enhanced in fig.2.2(c). Fig.2.2(d) is a weighted sum of the first ones and enhances diagonal edges. Concerning to the ridges, we can note that in non-structured areas the filter acts as a gaussian, while roots are enhanced.

2. Statistical Descriptors. Global descriptors are those that take into account the whole image interpreted as a random variable. The so called statistical moments are the quantities that measure the variability of a random variable. If dF_I is the probability density function of the random variable I and $\bar{I}$ denotes its mean value (zero order moment), then, the k order moment is given by:

$$m_k = \int (I - \bar{I})^k \, dF_I$$

In our case, if we consider the image as a random variable $I = I(i,j),\ i = 1,\ldots,n,\ j = 1,\ldots,m$, the k order moment is defined by:

$$m_k = \frac{1}{n \cdot m} \sum_{j=1}^{m} \sum_{i=1}^{n} (I(i,j) - \bar{I})^k, \quad \text{for} \qquad \bar{I} = \frac{1}{n \cdot m} \sum_{j=1}^{m} \sum_{i=1}^{n} I(i,j)$$

its mean value or mass center of the random variable I.

In particular we will focus on the second moment, that is the standard deviation of images com-

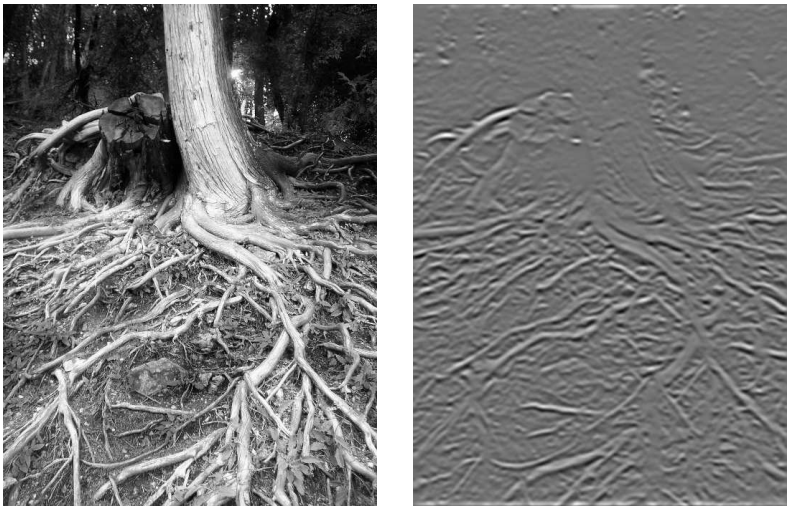

(a) (b)

Figure 2.3: Local Descriptors 2. Second derivatives as discontinuity measures for the computation of ridges.

paring the variability of gray level with the mean of the image. But we can be interested in the variability of a pixel with respect to the mean of the pixels of the same column or row. In a way, these measures can be oriented if the image presents a particular oriented pattern as figure 2.4 shows.

(a) (b) (c)

Figure 2.4: Global Descriptors. Oriented statistical measures from original image (a): Variance on vertical (b) and horizontal (c) direction.

In this image we compute the variance of original image (fig.2.4(a)) for each pixel. Notice the difference between computing the variance by columns (fig.2.4(b)) or by rows (fig.2.4(c)). If we compute the variance by columns (b), there is no variability along the first columns, so this results in a uniform gray value on the left side of the image in contrast with the right side, where there is the presence of the steps. On the other hand, in fig.2.4(c) we can note that, for each row, there is more variability on the wall side, comparing with the steps, that are more homogeneous. Concluding, we can speak of global edge detector, since it detects outstanding gray values.

By means of the descriptors, an image $I(i,j)$ is represented, only by its N characteristics $(X_l(I(i,j)))$ for $l = 1, \ldots, N$. These characteristics for a set of images make up point clouds in an N-dimensional space, the **Feature Space**.

2.2 Dimensionality Reduction

Depending on the dimensions of the feature space it is convenient reduce dimensionality to work better. Under the assumption of gaussianity of points clouds, the covariance matrix of the data contains information on the directions that best describe and/or discriminate objects. The former distinct goals give rise to two different criteria for dimensionality reduction:

- Object codification. The classic approach for object codification is Principal Component Analysis (PCA), which finds out a projection for the best description of the object. That is, PCA finds components that are useful for representing data based on the principal directions of the input data.
- Object discrimination. Multiple Discriminant Analysis (MDA) is the classic approach for object discrimination, in particular, Linear Discriminant Analysis (LDA), which searches a projection for the best discrimination of the different objects.

We note that the projection spaces yielded by PCA and Fisher Linear Discriminant (FLD) as a particular technique of LDA might be opposed, as we can see in figure 2.5. In this figure, we can observe the different behaviors of these techniques. If we seek for the principal direction of the data, we use PCA, whereas if what we want is to discriminate between the two classes, we use FLD. That is, FLD emphasizes the direction in which both classes can be better discriminated. It follows that PCA is more adequate for data representation and dimensionality reduction while FLD is better for feature classification. Since our aim is to discriminate the different structures we use Fisher Linear Discriminant.

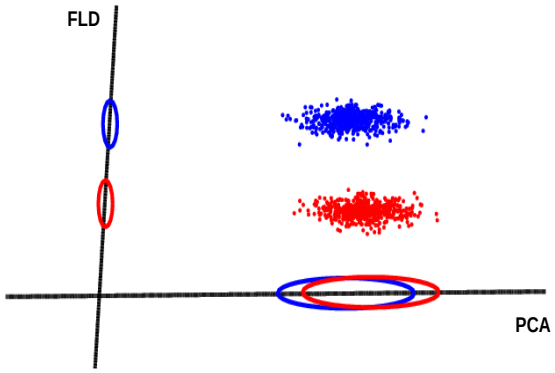

Figure 2.5: Fisher Linear Discriminant versus Principal Component Analysis. FLD seeks for the line achieving a maximum separability between classes while PCA finds out the principal direction of the whole data.

2.2.1 Fisher Linear Discriminant Analysis

Linear Discriminant Analysis searches for the linear subspace, W, that achieves a maximum separability among the projected classes. In the case of Fisher [35], separability is measured in terms of maximum separation between class means and minimum within-class scatter. Mathematically, this criterion is formulated in terms of the ratio between the between-class, S_B, and the within-class, S_W,

scatter matrices:

$$S_B = \sum_{i=1}^{c} (\mu_i - \mu)(\mu_i - \mu)^t$$

$$S_W = \sum_{i=1}^{c} \sum_{j=1}^{N_i} (Y_j - \mu_i)(Y_j - \mu_i)^t$$

for c the number of classes, μ_i the mean vector of each of them and μ the mean of all samples (Y_j). Fisher discriminant criterion reduces to finding the linear subspace, W, that maximizes:

$$J(W) = \frac{|W^t S_B W|}{|W^t S_W W|}$$

Because S_B encodes the projection onto the linear subspace given by $\mu_1, \ldots, \mu_c$, it has, at most, rank $c-1$, which bounds W dimension by $\dim W \leq c-1$. In the particular case of a 2-class problem in 2 dimensions, Fisher space is a straight line. Discrimination between the two classes corresponds to giving a threshold on the projection line, which induces a splitting of the feature space in two half planes, as we can observe in figure 2.5.

In fact, if we have two classes and the Fisher Linear Space, to classify is to find this threshold on the Fisher Linear Discriminant space. A standard way of finding the most suitable value is to use labelled samples to train a Bayes-like classifier.

2.3 Supervised Classification Techniques

Let (C_1, C_2) be the two classes of the problem projected onto the Fisher space, and f_1 and f_2 the respective density functions. In the pattern recognition framework, one of the classes is labelled as positives, P, and its counterpart as negatives, N. Then, true positives, TP, and true negatives, TN, refer to the data well classified and false negatives, FN, and false positives, FP, concern to the wrong classified data.

The aim of supervised classification techniques is to get a compromise between the proportion (probability) of false positives and false negatives. This compromise is achieved by means of cost functions which rely on the class concerning the proportion of FP and FN. Depending on the cost function, we can split these techniques in two approaches, Bayesian and precision-recall approaches.

2.3.1 Classic Bayesian Approach

The classic Bayesian strategy [35] searches for the value that achieves the minimum total error, that is, the percentage of false positives ($|FP|/|N|$) and false negatives ($|FN|/|P|$).

Given an observation vector X, our purpose is to determine whether X belongs to class C_1 or class C_2. The probability of error whenever we observe a particular X is:

$$P(error|X) = \begin{cases} P(C_1|X) & \text{if we decide } C_2 \\ P(C_2|X) & \text{if we decide } C_1 \end{cases} \tag{2.1}$$

where $P(C_i|X) = q_i(X)$ is the *a posteriori* probability, calculated from the *a priori* probability $P(C_i)$

and the *class-conditional density function* $p(X|C_i)$ using Bayes theorem:

$$q_i(X) = P(C_i|X) = \frac{P(C_i)p(X|C_i)}{p(X)} \tag{2.2}$$

where $p(X)$ is a mixture of Gaussians as a density function. Note that $p(X)$ is unimportant and we can eliminate this factor because it is positive.

Clearly, for a given X, and taking in mind the Bayes formula 2.2 we can minimize the probability of error by deciding C_1 if $P(C_1)p(X|C_1) > P(C_2)p(X|C_2)$ and C_2 otherwise, since Bayes decision rule minimizes the cost function:

$$P(C_1|X) + P(C_2|X) = P(C_1)p(X|C_1) + P(C_2)p(X|C_2) = P(C_1)P_1(FP) + P(C_2)P_2(FN)$$

if we refer P_1 for deciding C_1 and P_2 for deciding C_2

In this way, it is logical the following decision rule:

$$\begin{cases} X \in C_1 & \text{if} \quad q_1(X) > q_2(X) \\ X \in C_2 & \text{if} \quad q_1(X) < q_2(X) \end{cases} \tag{2.3}$$

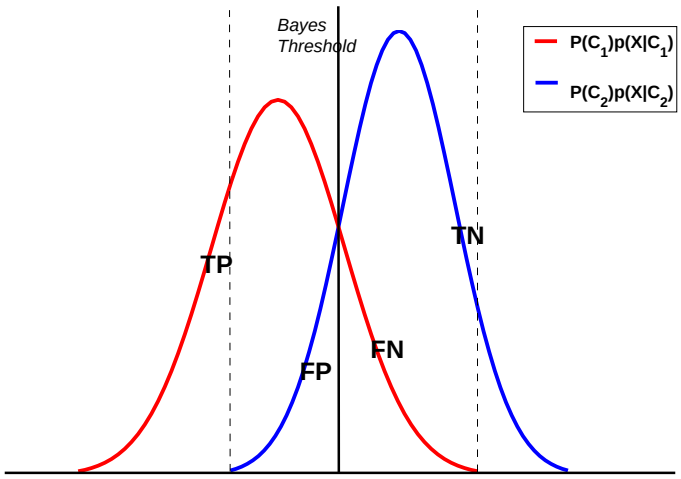

Figure 2.6: Bayes decision rule for minimum total error.

However, some kinds of classification mistakes can be more costly than others. For instance, what is more costly, to imprison an innocent or to free a guilty? Depending on the government they would prefer one choice or the other. In this case, the cost function is modified as:

$$\alpha_1 P_1(FP) + \alpha_2 P_2(FN) \tag{2.4}$$

where α_1 is the action corresponding the good decision of choosing C_1 and α_2 is the corresponding of choosing C_2.

Although the criterion is widely used in classification problems, in the context of object segmentation [37] it is more efficient to select thresholds in terms of the amount of noise, when the target object is a class extremely imbalanced compared to the rest of image pixels.

2.3.2 Precision-Recall Approaches

Bayes approach selects a threshold in terms of how many true positives are detected without considering the amount of noise introduced in the positive detections, that is, the fraction $|FP|/(|TP+FP|)$. In the information retrieval community, the standard evaluation criterion for noise tolerance are precision-recall curves, which measures the error in terms of how much true positives are required to succeed (recall), and how much noise can be tolerated (precision) [38].

As before, we can refer to figure 2.6 for a better understanding. Let P all the data labelled as C_1 class or "relevant" and N all the data labelled as C_2 class or "not-relevant". Let R be all the data classified as C_1, namely, "retrieved" and $\bar{R}$ its counterpart, "not-retrieved". From now, we can define TP the data retrieved and relevant, FP the data retrieved but not-relevant, FN the data not-retrieved but relevant and TN the data not-retrieved and not-relevant. It follows that precision is defined as the data retrieved and relevant over all the data retrieved, while recall is the data retrieved and relevant over all the data relevant as the following formulas show:

$$\text{PRECISION} = \frac{|TP|}{|TP+FP|} \qquad \text{RECALL} = \frac{|TP|}{|TP+FN|}$$

In probabilistic terms, precision is the probability that an object is relevant, given that it is retrieved, that is, an estimate of the conditional probability $P(C_1|R)$. Recall corresponds to the probability that a relevant object is retrieved, that is, an estimate of the conditional probability $P(R|C_1)$. Following the usual set-up in information retrieval, we define a decision rule in terms of our given observation vector X, to determine which data is classified as C_1 (the acceptance criterion). In this case the cost function is

$$\alpha_1 P_1(FN) + \alpha_2 P_2(FP)$$

Chapter 3

Deterministic Tools

Deterministic techniques involve those procedures determined by means of the minimum of an energy functional thoroughly described by image local characteristics and computed by means of an ODE or a PDE, which predict the behavior of the evolution of an initial quantity over time. In this chapter we explain the theoretical basis of these procedures.

3.1 Restricted Anisotropic Diffusion

Most filtering techniques based on image gray level modification [40], [41] use the heat diffusion equation:

$$I_t(x,y,t) = \mathrm{div}(J\nabla I) \quad \text{with} \quad I(x,y,0) = I_0(x,y) \tag{3.1}$$

to de-noise an image I_0. The time dependant function I is the family of smoothed images and J is a 2-dimensional metric that locally describes the way gray levels redistribute. The diffusion tensor J is thoroughly described by means of its eigenvectors (ξ, $\eta = \xi^{\perp}$) and eigenvalues (λ_1, λ_2). If the latter are strictly positive, like in existing anisotropic filtering techniques ([39], [41]), gray values spread on the whole image plane and the family I converges to a constant image. But if we degenerate J and admit null eigenvalues ($\lambda_2 = 0$), then diffusion only takes place in the integral curves of the eigenvector (ξ) of positive eigenvalue [34]. Smoothing effects depend on the suitable choice of the eigenvector of positive eigenvalue. In the case that ξ is a smooth vector representing the tangent space to a closed model of the image level sets, then the final image is a collection of curves of uniform gray level [33].

The Structure Tensor [44] is a quick way of computing the guiding vector ξ that has already proven its efficiency [34]. The Structure Tensor, namely ST_ρ, is a gaussian mean of the projection matrices onto a regularized image gradient. That is, given a gaussian, G_ρ, of variance ρ and zero mean, the structure tensor is the following convolution:

$$ST_\rho = G_\rho * \left[\begin{pmatrix} I_x \\ I_y \end{pmatrix} (I_x, I_y) \right] = \begin{pmatrix} G_\rho * I_x^2 & G_\rho * I_x I_y \\ G_\rho * I_x I_y & G_\rho * I_y^2 \end{pmatrix}$$

for $(I_x, I_y) = G_\sigma * \nabla I$ the components of a regularized image gradient. Since, ST_ρ is the solution to the heat equation with initial condition the projection matrix onto the image gradient, its eigenvectors are infinitely differentiable fields that regularize and approximate the image level sets tangent and normal

spaces. We use ST_ρ eigenvectors to design our diffusion tensor as follows.

Let us consider a metric $\tilde{J}$ with eigenvalues $\lambda_1 = 1$ and $\lambda_2 = 0$, and ξ the eigenvector of minimum eigenvalue of ST_ρ. The Restricted Heat Diffusion we suggest is given by:

$$\begin{aligned} & I_t = \operatorname{div}(Q\tilde{\Lambda}Q^t\nabla I), \quad I(x,y,0) = I_0(x,y) \\ & \text{with } Q \text{ the eigenvectors of } ST_\rho = G_\rho * \left(\nabla I_\sigma \nabla I_\sigma^T\right), \\ & \tilde{\Lambda} = \begin{pmatrix} 0 & 0 \\ 0 & 1 \end{pmatrix} \quad \text{and} \quad \nabla I_\sigma = G_\sigma * \nabla I \end{aligned} \tag{3.2}$$

By setting the smoothing parameters to $(\sigma, \rho) = (0.5, 2)$, ξ yields a closed approximation of the image level sets tangent space around continuous structures, meanwhile at noisy areas is an irregular vector with random orientation. It follows that the above procedure smoothes image gray values along its regular structures and acts like a gaussian filter otherwise.

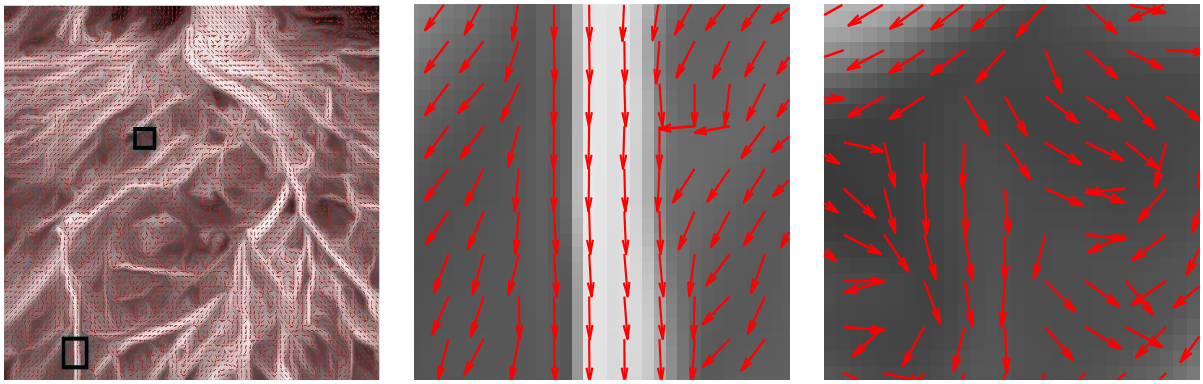

(a) (b) (c)

Figure 3.1: Vector field of RAD (a) and a zoom of a regular vector field area (b) and a random vector field area (c).

Figure 3.1 illustrates the grounds of equation (3.2). The vector ξ depicted in both images define the direction to smooth. Near regular structures (fig.3.1(a)) ξ is well defined and continuous, whereas at noisy areas (fig.3.1(b)) it is randomly distributed. The result is that solutions to (3.2) converge to a smooth image that enhances the main features of the original image, in the sense that their response to standard detectors based on the image local characteristics is uniform. This filtering scheme modifies classic anisotropic diffusions [41] by suppressing any diffusion across image level curves since the associated image operator homogenizes image structures gray values according to their geometric continuity. This results in a more uniform continuous response of RAD filtered images to detectors based on local descriptors (edges, valleys, ridges) of image gray values as we can note in figure 3.2.

Figure 3.2 illustrates the effects of the equation (3.2) in a natural image and compares it with the effects of the anisotropic filtering of Weickert. We applied a ridge detector based on the curvature [42] in original image (fig.3.2(a)), Weickert filtered image (fig.3.2(b)) and RAD image (fig.3.2(c)) by computing the positive values of a robust unit gradient of each image, im: $\kappa = -\operatorname{div}(\nabla im)$. This ridge detector is noise sensitive, since it bases on the normalized gradient vector of each image. As we can see, the original response (fig.3.2(d)) yields fragmented curves for the target structures and fake detections due

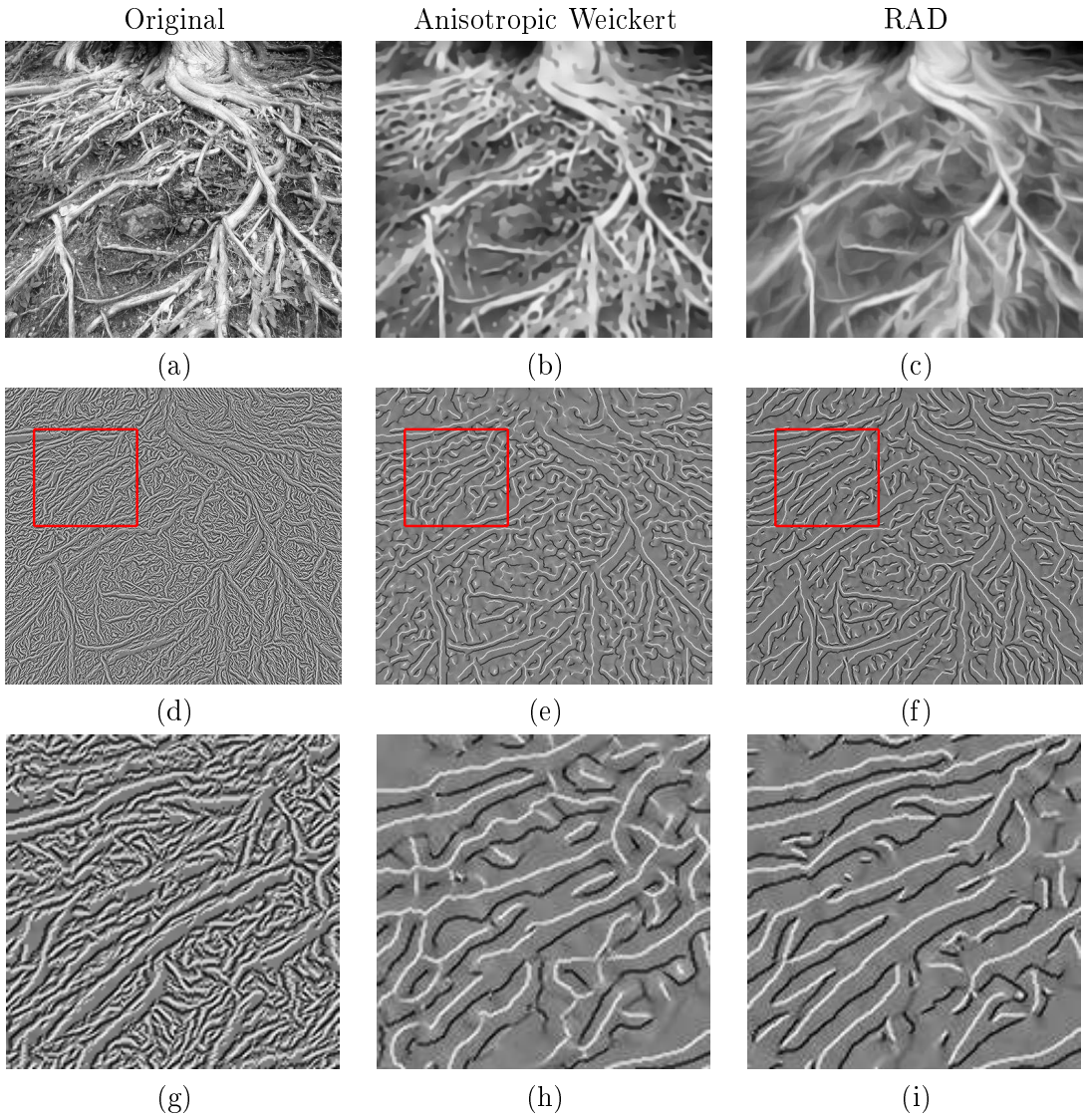

Figure 3.2: Ridges on different smoothed images. Original smoothed images (a), (b), (c), their corresponding ridges (d), (e), (f) and a zoom of these ridges (g), (h), (i).

to noise. Weickert filtered response (fig.3.2(e)) still presents these drawbacks, while in RAD response (fig.3.2(f)), background spurious ridges have been removed whereas roots are continuous closed curves.

3.2 Implicit Anisotropic Contour Closing

Heat diffusion has the property of smoothly extending a function defined on a curve in the plane, provided that boundary conditions are changed to Dirichlet [43]. By using restricted heat operators this property can be used to complete unconnected contours [34] as follows.

Let γ_0 be the set of points to connect, χ_{γ_0} its characteristic function (a mask) and define $\tilde{J}$ as in

RAD (3.2). Then, the extension process:

$$I_t = \mathrm{div}(\tilde{J}\nabla I) \quad \text{with} \quad I_{|\gamma_0} = \chi_{\gamma_0} = \begin{cases} 1, & \text{if the pixel belongs to } \gamma_0; \\ 0, & \text{otherwise.} \end{cases} \tag{3.3}$$

converges to a closed model of γ. Intuitively, we are integrating the vector field ξ, that is, we are interpolating the unconnected curve segments along it. This fact contribute two main advantages: first, the use of a restricted heat equation (3.3) ensure convergence to a closed model of the unconnected curve, whatever its concavity is. Second, because ξ takes into account image level sets geometry ACC closures are more accurate than other interpolating techniques (such as geodesic snakes [36]) which, at most, yield piece-wise linear models.

In order to avoid wrong continuations at noisy areas, the vector ξ is weighted by the coherence of the Structure Tensor. This quantity measures the vector regularity and is given by:

$$coh = \frac{(\lambda_1 - \lambda_2)^2}{(\lambda_1 + \lambda_2)^2}$$

for $\lambda_1 \geq \lambda_2$, ST_ρ eigenvalues. At regions where ξ is a continuous vector, λ_2 is closed to zero, so coh is maximum, meanwhile, at noisy areas, since ξ is randomly oriented, λ_1 compares to λ_2 and $coh \sim 0$.

The vector guiding ACC is defined by:

$$\xi = coh\,\tilde{\xi} \quad \text{for} \quad \tilde{\xi} = minEig(ST_\rho(I)) \tag{3.4}$$

(a) (b) (c)

Figure 3.3: Anisotropic Contour Closing. Original image (a), mask to be closed (b) and the final result (c).

Figure 3.3 shows the result of the algorithm. The mask from the original image (fig.3.3(a)) to be closed is drawn in white in fig.3.3(b) and the result is shown in fig.3.3(c).

3.2.1 Quick Anisotropic Contour Closing

For the sake of a computational cost as small as possible, we use the following quick algorithm for solving equation (3.3). First recall that the final image yielded by ACC is a mask (i.e. 1's and 0's) of the closed curve and that the whole process might be regarded as integrating the field ξ. Remember we seek for solutions to the following extension problem:

$$\mathrm{div}(\tilde{J}\nabla I) = 0 \quad \text{with} \quad I_{|\gamma_0} = \chi_{\gamma_0}$$

For a better understanding, we refer to heat equation 3.1. Let us consider our image I as a mass distribution. The vector field $\vec{j} = \tilde{J}\nabla I$ locally describes the direction towards the initial mass move. On one hand, concerning the final heat distribution, steady states of (3.1) can be described by means of their level sets. On the other hand, in the basis $\{\xi, \xi^{\perp}\}$, $\tilde{J}\nabla I$ develops as:

$$\tilde{J}\nabla I = \lambda_1 \langle \nabla I, \xi \rangle \xi + \lambda_2 \langle \nabla u, \xi^{\perp} \rangle \xi^{\perp} = \langle \nabla I, \xi \rangle \xi$$

so, if we denote by Ω the region enclosed by a level curve γ then, $\vec{j} = \langle \xi, \nabla u \rangle \xi$ is tangent to γ. It follows that the Divergence formula yields that the evolution of I_t fulfils:

$$\int_{\Omega} I_t = \int_{\Omega} \mathrm{div}(j) = \int_{\gamma} \langle \vec{j}, \xi \rangle$$

Since our initial mask γ_0 belongs to a level curve and the effect of the diffusion redistributes the mass along it, we have that, for each border point of a segment, the next pixel to be set to 1 is the neighbor in the direction ξ (cross in fig.3.4(b)). Such pixel achieves the maximum correlation between ξ and the gradient of the distance map to the uncomplete curve (dot in fig.3.4(c)). In this manner the whole closing process is of the order of the gap (pixel) size.

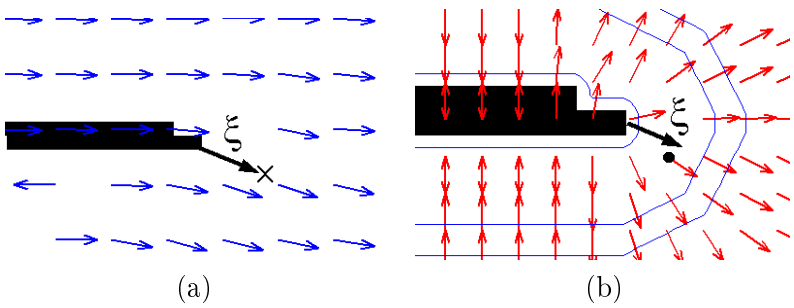

Figure 3.4: Quick Anisotropic Contour Closing.

Figure 3.4 illustrates the grounds of the quick algorithm: For an unconnected segment, fig.3.4(a) shows the vector to be integrated and fig.3.4(b) the distance map gradient used to compute ACC.

3.3 B-snakes

A parametric snake is a curve $\gamma(u) = (x(u), y(u))$ which, under the influence of an external force, E_{ext}, and internal constrains, E_{int}, minimizes the energy functional:

$$\begin{aligned} E(\gamma) &= \int_{\gamma} (E_{int}(\gamma) + E_{ext}(\gamma, \gamma_\tau)) du \\ &= \int_{\gamma} (\frac{1}{2}\alpha \|\dot{\gamma}\|^2 + \frac{1}{2}\beta \|\ddot{\gamma}\|^2 + E_{ext}(\gamma, \gamma_\tau)) du \\ &= \int F(\gamma, \dot{\gamma}, \ddot{\gamma}) du \end{aligned} \tag{3.5}$$

where γ_τ is the target curve to model and $\alpha, \beta \in [0, 1]$ weight the trade off between the elasticity and stiffness of the snake. The external energy is an external potential achieving a minimum on γ_τ.

The Euler-Lagrange equation of E, given by

$$F_\gamma - d_u(F_{\dot{\gamma}}) + d_{uu}(F_{\ddot{\gamma}}) = 0$$

leads to solving a system of 2 equations in the continuous domain:

$$-\alpha x_{uu} + \beta x_{uuuu} + \frac{\partial E_{ext}}{\partial x} = 0$$

$$-\alpha y_{uu} + \beta y_{uuuu} + \frac{\partial E_{ext}}{\partial y} = 0$$

In the discrete case γ is defined as $\gamma = (x_1, \ldots, x_n, y_1, \ldots, y_n)$ and the energy functional is defined by:

$$E = \sum_{i=1}^{n} E_{int}(i) + \sum_{i=1}^{n} E_{ext}(i)$$

The corresponding Euler-Lagrange equations are a system of 2N equations which can be written in a matrix form:

$$Ax = -\frac{\partial E_{ext}}{\partial x} \qquad Ay = -\frac{\partial E_{ext}}{\partial y} \tag{3.6}$$

where A is a pentadiagonal matrix called the stiffness matrix and expressed by:

$$\begin{pmatrix}
2\alpha+6\beta & -\alpha-4\beta & \beta & 0 & 0 & 0 & \ldots & \beta & -\alpha-4\beta \\
-\alpha-4\beta & 2\alpha+6\beta & -\alpha-4\beta & \beta & 0 & 0 & \ldots & 0 & \beta \\
\beta & -\alpha-4\beta & 2\alpha+6\beta & -\alpha-4\beta & \beta & 0 & 0 & \ldots & 0 \\
0 & \beta & -\alpha-4\beta & 2\alpha+6\beta & -\alpha-4\beta & \beta & 0 & \ldots & 0 \\
\vdots & \vdots & \vdots & \vdots & \vdots & \vdots & \vdots & \vdots & \vdots \\
-\alpha-4\beta & \beta & 0 & 0 & \ldots & 0 & \beta & -\alpha-4\beta & 2\alpha+6\beta
\end{pmatrix}$$

The iterative solution for the minimization is similar to the general one for linear systems:

$$Ax = -\frac{\partial E_{ext}}{\partial x} \qquad Ay = -\frac{\partial E_{ext}}{\partial y}$$

and may be written as:

$$(A+\gamma I)x = \gamma x - \frac{\partial E_{ext}}{\partial x} \qquad (A+\gamma I)y = \gamma y - \frac{\partial E_{ext}}{\partial y}$$

for any scalar γ. Thus we have:

$$x = (A+\gamma I)^{-1}(\gamma x - \frac{\partial E_{ext}}{\partial x}) \qquad y = (A+\gamma I)^{-1}(\gamma y - \frac{\partial E_{ext}}{\partial y})$$

and the recurrent equation is given by:

$$x_{t+1} = (A+\gamma I)^{-1}(\gamma x_t - \frac{\partial E_{ext}}{\partial x}) \qquad y_{t+1} = (A+\gamma I)^{-1}(\gamma y_t - \frac{\partial E_{ext}}{\partial y})$$

Chapter 4

Adventitia Modelling Steps

4.1 General Strategy

The strategy for adventitia segmentation we suggest is a three fold algorithm summarized as follows:

1. IMAGE PREPROCESSING

   (a) **Polar Transformation of IVUS images**

   Advanced techniques for medical imaging segmentation [30] use *a priori* knowledge of the target structure shape. Active shape contours [31] are the usual way to incorporate such knowledge to the model. In the case of the adventitia border, its circular appearance can be imposed by simply transforming images to polar coordinates with the origin at the geometric center of the vessel border. In this coordinate system, the adventitia transforms into a horizontal curve, which significantly simplifies border feature extraction.

   (b) **Restricted Anisotropic Diffusion (RAD)**

   IVUS images are particularly noisy, as well as, in most of cases, adventitia appears as a very weak contour, so, in order to enhance significant structures while removing noise and textured tissue, we use a Restricted Anisotropic Diffusion [33] detailed in Section 3.1. As we saw, it results in a more effective operator than classic anisotropic diffusions ([39],[41]), which, since they rely on such local descriptors, restrict their smoothing effect to a particular structure.

2. STATISTICAL SELECTION OF BORDER POINTS

   The goal of our classification stage is to compute two binary images (masks), one for vessel borders segments and another for calcium sectors. Extracting vessel borders and calcium points requires defining the functions that best characterize each set, as well as, their most discriminating values. We learn, both, feature space and parametric threshold values by applying supervised classification techniques to a training set of manually segmented images.

   (a) **Feature Space Design**

   Our feature space is designed to discriminate among the set adventitia/intima, calcium and fibrous tissue. Calcium discrimination is needed to discard angular sectors of ambiguous

information and fibrous tissue to avoid miss detections of vessel borders. By the polar coordinate system chosen, horizontal edges are the main descriptors of the set adventitia/intima. Image simple statistics (standard deviation and cumulative means) serve to formulate the functions characterizing calcium and fibrous plaque.

(b) **Extraction Parameters**

Recall that in a segmentation procedure there are two kind of parameters. For thresholding parameters, if the segmentation problem is especially concerned with the noise introduced, precision-recall approaches are more accurately than classical Bayes approach. For filtering parameters, we detailed in Subsection 5.2 why we use a length filtering on the extracted segments to remove spurious detections due to artifacts. Thresholding and filtering parameters are tuned to yield an optimal segmentation for a training set of manually traced borders.

3. SEGMENTATION STAGE

The selection stage produces two binary images: adventitia/intima points and calcium sectors. Vessel border segments are modelled by computing an implicit closed representation and, then, an explicit snake representation using B-splines.

(a) **Implicit Anisotropic Contour Closing (ACC)**

For the implicit closing we suggest using an Anisotropic Contour Closing [34] based on functional extension principles to complete curve segments in the image mask domain. The use of restricted diffusion operators enables to take into account image geometry and discard calcium and side branches sectors. Since ACC interpolates line segments along image level curves, the implicit reconstruction provides with a faithful closed model of vessel borders.

(b) **Explicit B-Snakes Representation**

Gaps at calcium sectors and side branches are completed by using B-spline snakes to interpolate ACC radial values in the polar domain. In the cartesian domain the final smooth model yields an elliptical shape at sectors where no information is available. In this way the compact B-spline representation yields a model that matches the Gestalt principles of good continuation.

4.2 Image Preprocessing

4.2.1 Polar Coordinates

The fact that, in an IVUS plane, adventitia is a circular shaped structure (fig.4.1(a)) suggests transforming images to polar coordinates. If $I(x, y)$ denotes the image in the cartesian domain then, its polar transform, $IPol(r, \theta)$, is given by the formula:

$$\begin{aligned} X(r,\theta) &= x_0 + r\cos\left(\frac{\theta\pi}{180}\right) \\ Y(r,\theta) &= y_0 + r\sin\left(\frac{\theta\pi}{180}\right) \\ IPol(r,\theta) &= IPol(X(r,\theta), Y(r,\theta)) \end{aligned}$$

where the radius and angle are in the ranges $r \in [0, R_{max}]$ and $\theta \in [0, 360)$ and (x_0, y_0) is the origin of coordinates.

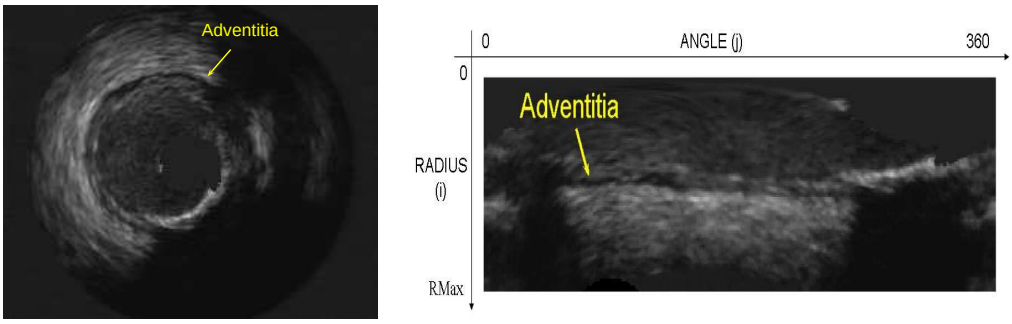

(a) (b)

Figure 4.1: Adventitia images in cartesian (a) and polar coordinates (b).

In this coordinate system, the adventitia layer appears as a horizontal dark line (fig.4.1(b)) provided that (x_0, y_0) is its geometric mass center. Any deviation introduces an undulation in the polar transform of the vessel structure (fig.4.2(a)), which forces the use of oriented filters for feature extraction based on image local descriptors (e.g edges). Besides the artifact caused by geometric eccentricity, in non ECG-gated sequences, one has to compensate the transformations induced by cardiac movement. Cardiac dynamics introduce two main rigid transformations: a translation of the vessel followed by a rotation centered at the vessel center. In a polar domain with a fixed origin (e.g. the image center), the former transformations result in a dynamic radial wave (due to translation) followed by a horizontal (angular) translation. The first one is a main artifact for a temporal analysis of the block of images that constitute an IVUS sequence since it strongly modifies the vessel border geometry. We straighten the adventitia border as follows.

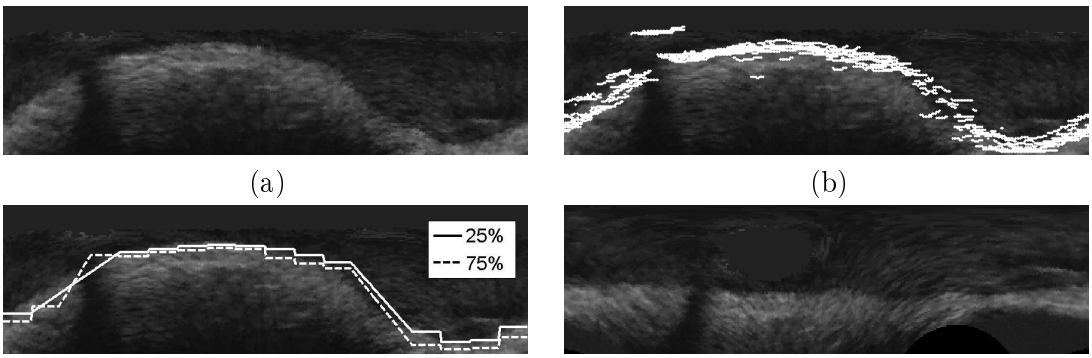

(a) (b)

(c) (d)

Figure 4.2: Adventitia Straighten Procedure: polar image with origin at the image mass center (a), edges in a sequence block (b), central percentile of edges positions (c) and final polar image (d).

Heart dynamics eccentricity is removed by taking as origin the image mass center. Still, in such polar system (fig. 4.2(a)) the adventitia might present a static curved pattern if the vessel is not centered at the physic image center. This geometric eccentricity is reduced by computing the geometric mass center of a set of points roughly lying on the adventitia. Such points are extracted by means of negative horizontal

edges, namely e_y. The impact of noise and artifacts is minimized by considering the average of e_y for a block of N sequence frames. We select for each angle (column) those points with the former average below the 5% radial percentile. Spurious edges due to noise and other sparse artifacts are removed by applying a length filtering to the extracted edges. In order to endow further continuity to the selected segments, we use the statistical distribution of their radial position along a block of images. Percentiles computed in the sequence block serve to discard outliers by only considering points within the central percentile range. In order to capture the adventitia curvature, percentiles are computed on angular sectors of 5 angles. The final radial values serve to compute the new origin of our polar transform.

Figure 4.2 illustrates the main steps of the geometric eccentricity suppression. Fig. 4.2(a) shows the polar transform with the origin at the image mass center. In fig.4.2(b) we show the selected edges in a sequence block before percentile filtering and fig.4.2(c) shows the plot for their central percentile. The straighten adventitia image is shown in fig.4.2(d).

From now on, we will work with images in polar coordinates. We will note $AdvPol(i, j)$ the discrete polar transform of an IVUS frame, for the radius, i, and the angle, j, given by:

$$i = 1, \ldots, \min(Nc, Nr) \quad \text{and} \quad j = 1, \ldots, 360$$

where Nc, Nr are the dimensions (columns and rows) of the original IVUS image.

4.2.2 Restricted Anisotropic Diffusion

As we explained in section 3.1 Restricted Anisotropic Diffusion (RAD) is a useful tool for preprocessing IVUS images and aid the selection of target structure points with statistical tools by de-noising images. An important point is that the process is totally automatic and it stops when the image is de-noised but structures are enhanced, that is, when the diffusion stabilizes. Nevertheless, one drawback of this procedure is the computational cost since it is an iteratively process and it is applied on the whole image. In order to reduce this cost, we apply RAD in a band of interest containing the adventitia layer and achieving a reduction of 50% of computational time. This band, obtained by an automatic ROI selection, contains all the pixels between the minimum of the 25 percentile and the maximum of the 75 percentile plus a reasonable interval of pixels. Figure 4.3 shows an original IVUS image transformed in polar coordinates (fig.4.3(a)) and the corresponding filtered image (fig.4.3(b)).

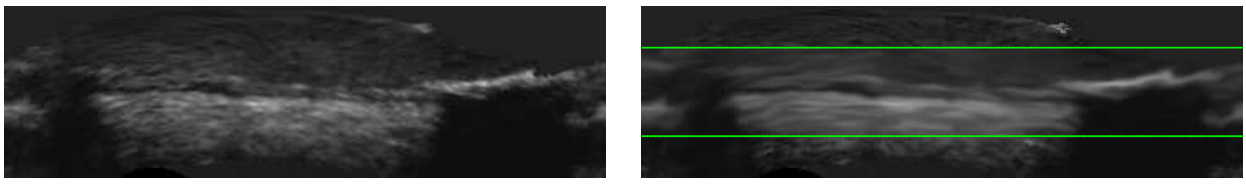

(a) (b)

Figure 4.3: Image Preprocessing: polar transformation (a) and RAD filtering in a band (b).

4.3 Statistical Selection of Border Points

The inner and outer vessel borders appearance is so similar that they are assumed to constitute a single class in the training process. Their distinct radial position suffices to discriminate them [22] in the absence of echo opaque structures, such as calcium. In such cases, the adventitia does not appear and the detection is misled towards the intima. Since the best solution is to discard echo opaque sectors, the training stage also addresses their characterization. We also include fibrous tissue discrimination because it is a main artifact confusing with the adventitia that forces the use of longitudinal cuts [22].

For linguistic simplicity, echo opaque structures will often be referred to as calcium.

4.3.1 Feature Space

Based on visual perception, we mainly distinguish adventitia/intima by horizontal edges and echo opaque structures by their shadow underneath. Let $AdvPol$ and (i, j) be the image in polar coordinates and their pixel position respectively. The feature space we propose is a three dimensional space tuned to describe the adventitia/intima set and echo opaque structures.

1. *Horizontal Edges*

   Since in the coordinate system chosen, the adventitia layer is a horizontal dark line, horizontal edges constitute our main descriptor. Edges are computed by convolving the image with the y-partial derivative of a 2 dimensional gaussian kernel of variance ρ:

   $$\begin{aligned} &e_y(i,j) = g_y * AdvPol \\ &\text{for} \quad g_y(i,j) = -\tfrac{j}{2\pi\rho^4} e^{-(i^2+j^2)/(2*\rho^2)} \end{aligned}$$

   The only image structures yielding large values for e_y are intima, adventitia, calcium and fibrous tissue. Intima and adventitia correspond to negative values, while calcium and fibrous structures yield a negative and a positive response, one for each of their bordering sides.

   The descriptors we have chosen to detect echo opaque plaques and fibrous tissue are their outstanding brightness and, for calcium, the dark shadow underneath. We propose the following particular functions to quantify such features.

2. *Radial Standard Deviation*

   Striking brightness corresponds to an outlier of the pixel gray value in the radial distribution. We measure it by means of the difference between the pixel gray value and the radial mean. For each pixel (i, j), we define it as

   $$\sigma(i,j) = (AdvPol(i,j) - \nu(\theta))^2$$

   where $\nu(\theta))$ is the radial (i.e. column-wise) mean of the polar image:

   $$\nu(\theta) = \frac{1}{R_{max}} \sum_{i=1}^{R_{max}} AdvPol(i,\theta)$$

   The magnitude of σ is maximum at bright structures (calcium and fibrous plaque) and minimum near the adventitia. In order to distinguish between calcium and fibrous plaque, we add the following shadows detector:

3. *Cumulative Radial Mean*

   For each angle j consider the following cumulative mean:

$$CS_j(i) = \frac{\sum_{n=R_{max}}^{n=i} AdvPol(n,j)}{R_{max} - i}$$

   For angles with calcium, the function $CS_j(i)$ presents a step-wise profile in contrast to a more uniform response in the presence of fibrous plaque. It follows that the total energy:

$$ecs(j) = \sum_{i=1}^{i=R_{max}} CS_j(i)$$

   achieves its minimum values only at angles with calcium.

The feature space achieving a maximum separability for our training set is given by:

$$(X, Y, Z) = (e_y, sign(e_y)\sqrt{|e_y \sigma|}, ecs) \tag{4.1}$$

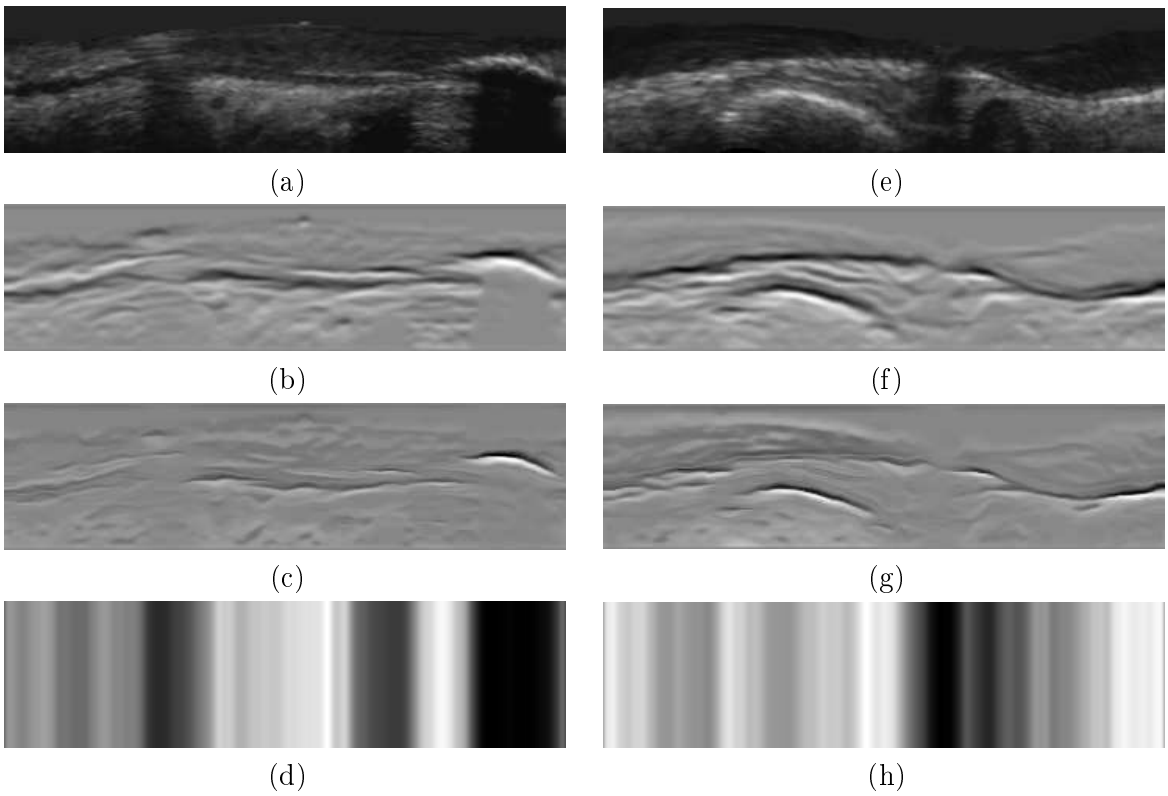

Figure 4.4: Image descriptors. Original images (a),(e) and Vessel Structures Descriptors: Horizontal Edges (b),(f), Radial Standard Deviation (c),(g) and Cumulative Radial Mean (d),(h).

Figure 4.4 shows the feature space for a calcified (1st column) and normal (2nd column) cross-sections. The original images are in the first row, energy from the first derivative in vertical direction in the second row, Radial Standard Deviation in the third and Cumulative Radial mean in the fourth row. From *ey* energy images (fig.4.4(b),(f)) we extract negative horizontal edges. Radial Standard

Deviation (fig.4.4(c),(g)) shows a maximum in calcium sectors (fig.4.4(c)),and fibrous plaques (fig.4.4(g)) and finally, Cumulative Radial Mean (fig.4.4(d),(h)) shows a minimum in calcium sectors (last columns in fig.4.4(d)) and angles with lack of information (middle columns in fig.4.4(h)).

4.3.2 Statistical Parameter Setting

For the computation of the vessel borders and calcium binary images, the classification problem we must face is discriminating among 4 different sets: adventitia/intima (Adv), calcium (Cal), fibrous structures (Fbr) and the rest of pixels (RP). Instead of addressing the 4-class problem as a whole, we will solve several 2-class problems in 2 dimensions.

For its simplicity and proven efficient performance, Fisher linear discriminant analysis [35] explained in subsection 2.2.1 serves to reduce dimensionality of the feature spaces. Either for vessel borders mask or calcium mask the Fisher space is a straight line (see fig.4.5(a)). Discrimination between the two classes corresponds to giving a threshold on the projection line (line labelled τ_{PF1} in fig.4.5(b)), which induces a splitting of the feature space in two half planes. For the vessel borders mask, we will use a Bayesian approach [35] to select thresholding values, since miss classifications will be discarded with filtering parameters. For the calcium mask, we will use precision-recall curves to select such threshold.

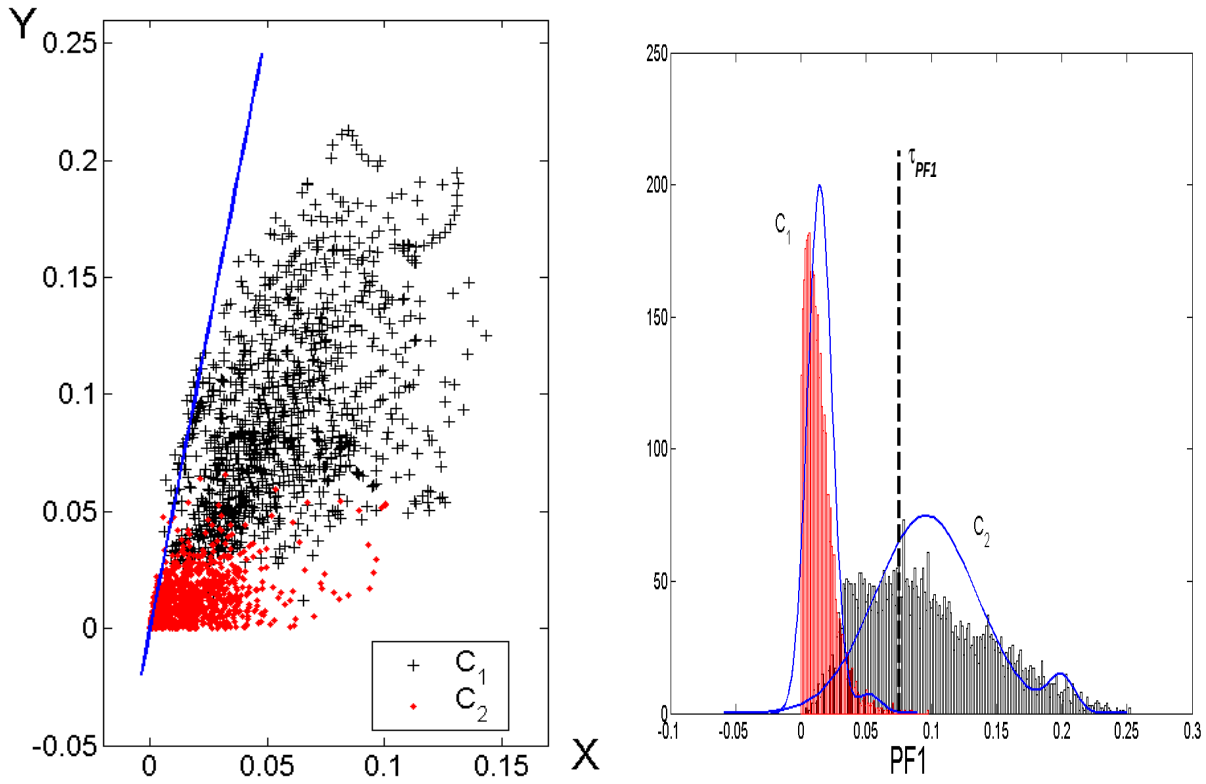

Figure 4.5: Adventitia/Intima vs Calcium/Fibrous Tissue sets Discrimination. Feature Space (a) and discrimination on the Fisher Projection Line (b)

This is the strategy we propose for the computation of the Adv and Cal mask images.

A. **Vessel Borders Mask.**

Borders extraction is achieved by addressing 2 classification issues: discriminate C_1=(Adv,RP) and C_2=(Cal, Fbr) in the (X, Y) plane and, then, separate Adv from RP using X values.

We remind that Adv, Cal and Fbr are the only tissues yielding large response for X values. It follows that the clustering proposed (C_1, C_2) ensures that after discriminating between Adv and RP, the set classified as Adv will not include any other structures but vessel borders. This avoids the use of longitudinal cuts [22] to distinguish between intima and adventitia, since they are directly identified by their radius.

We discriminate C_1 (positives) and C_2 (negatives) by projecting onto the Fisher space, $PF1$, (see fig.4.5(a)). Since our discriminating problem is detecting as much points on the adventitia as possible, we tune the standard Bayesian threshold in order to achieve a maximum number of true C_1 detections regardless of false positives (see fig.4.5(b)). Such miss classifications are discarded in the subsequent discriminating and filtering steps. Among all thresholds ensuring at least 90% of true C_1 detections, we choose the value, τ_{PF1}, that, in combination with the rest of parameters, yields optimal segmentation results. Figure 4.5 summarizes the main steps of the discrimination between C_1 and C_2. Figure 4.5(a) shows the feature space chosen and the Fisher projection line. Figure 4.5(b) the projected classes onto $PF1$ and a threshold discriminating line τ_{PF1}.

Discrimination between Adv and RP is achieved in the X coordinate domain, as Adv corresponds to large negative values. Large range of Adv values among different patients, suggests the use of an image sensitive threshold rather than a common value for all cases. We adopt a strategy in the fashion of discriminant snakes [26], [28] and select a different value for each column. Radial (column-wise) percentiles (ρ_X) are used to compute such threshold. Finally, small structures in the vessel borders image can be removed by applying either a length or an area filtering. Although a length filtering is more flexible some 3D continuity might be lost. In contrast, an area filtering is fixed for all frames but takes into account 3D continuity. In our case, we use a length filtering, so that only segments of length above a given percentile (ρ_F) are kept.

If we note by $PF1$ the projection of the (X, Y) space onto the Fisher line, then, for every frame, points are labelled as Adv if they fulfill:

$$PF1 < \tau_{PF1}, \qquad X < \rho_X$$

and their segment length is above ρ_F.

Figure 4.6 illustrates the extraction of adventitia/intima points. In fig.4.6(a) we have the output of the discrimination step and in fig.4.6(b) the result after applying a length filtering.

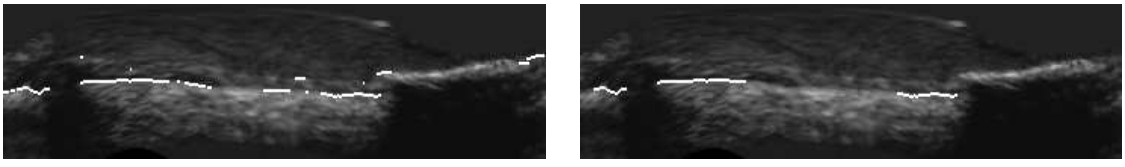

(a) (b)

Figure 4.6: Vessel Borders Point Extraction (1). Adventitia mask resulting from the classification (a) and the final one after length filtering (b)

B. **Calcium Mask.**

The feature space chosen to discriminate calcium from fibrous tissue is given by the projection $PF1$ and the Z coordinate. A threshold on the Fisher space, $PF2$, for the 2D space $(PF1, Z)$ separates Cal and Fbr. Instead of following a Bayesian approach we will consider precision-recall curves (figure 4.7) to select thresholding values, as we can not run the risk of identifying too much Fbr and artifacts (noise) as calcium.

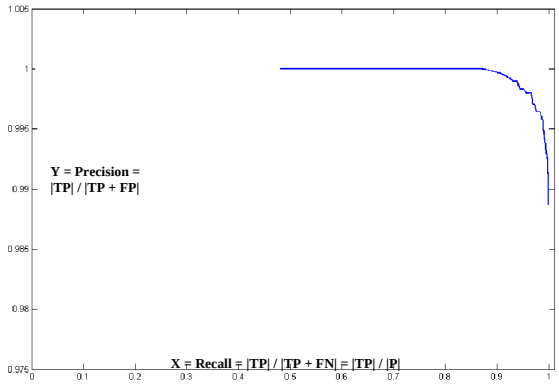

Figure 4.7: Precision-Recall curve to select thresholding values for the computation of calcium mask

As in the computation of the vessel borders mask, we tune thresholding values and among all thresholds admitting, at most, a 10% of noise , we choose the value, namely τ_{PF2}, that ensures a better segmentation of our training set.

It follows that, calcium points are those pixels that satisfy:

$$PF1 \geq \tau_{PF1} \quad \text{and} \quad PF2 > \tau_{PF2}$$

Figure 4.8 shows the points classified as calcium in white.

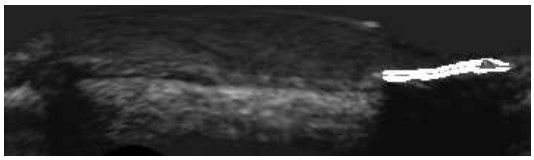

Figure 4.8: Vessel Borders Point Extraction (2). Calcium mask

The thresholding parameters (τ_{PF1}, ρ_X, ρ_F and τ_{PF2}) hinge on the ultrasonic acquisition device characteristics. The specific values for the device used in our experiments are given in the experimental Section 5.2.

4.4 Closing Stage

The selection stage produces two mask (binary) images: one for calcium and another one for vessel borders. The latter is a collection of fragmented curve segments (fig.4.9(b)), which are closed in 2

steps. First we complete them in the mask image domain by an interpolation process based on extension principles. Then, an explicit snake is used to compute a B-spline model of the adventitia.

4.4.1 Anisotropic Contour Closing

For adventitia completion we use the numeric approximation given in 3.2.1. The vector ξ is the eigenvector of minimum eigenvalue of the Structure Tensor computed over the edge map e_y. The main artifacts to obtain a reliable closed model are side branches, sensor shadows and calcium sectors. Side branches and sensor shadows can be considered noisy areas, so it had been taken into account in (3.4). However, calcium sectors are not noisy areas but in general are continuous to the adventitia. In order to avoid this wrong continuation, we modify the weight in (3.4) by a function w_ξ. Now, the weight is set to zero at calcium sectors and to the value of the coherence of the Structure Tensor otherwise. The vector guiding ACC is modified as follows:

$$\xi = w_\xi \tilde{\xi} \quad \text{for} \quad \tilde{\xi} = minEig(ST_\rho(e_y))$$
$$\text{and} \quad w_\xi(i,j) = \begin{cases} 0, & \text{if } (i,j) \in \text{Calcium} \\ coh, & \text{otherwise} \end{cases}$$

After ACC closing we apply an area filtering in the same fashion as in the above selection stage in order to endow the model with 3D continuity.

4.4.2 B-snakes

Since the above interpolation still presents gaps at side branches and calcium sectors, we guide a parametric B-snake towards ACC closure in order to close them and obtain a compact explicit representation by B-splines. The general iterative procedure given in subsection 3.3 significantly simplifies in our particular case.

In polar coordinates, any curve γ is given by $\gamma(s) = (\theta(s), R(s))$ and can be, indeed, parameterized by θ, as $\gamma = \gamma_\theta = (\theta, R(\theta))$. It follows that the functional (3.5) simplifies to:

$$\begin{aligned} E(R(\theta)) &= \int_0^{360} E_{int}(R_\theta, R_{\theta\theta}) + E_{ext}(R, R_\tau) d\theta \\ &= \int_0^{360} (\alpha \|R_\theta\|^2 + \beta \|R_{\theta\theta}\|^2 + (R - R_\tau)^2) d\theta \end{aligned} \tag{4.2}$$

for R_τ the radius of the target curve. We parameterize R by a B-Spline given by N control points (R_i, θ_i) where $\theta_i = \frac{360i}{N}$, $i = 1, \ldots, N$. Given that θ_i are uniformly spaced, $\theta(s) = \sum_i c_i(s)\theta_i$ is a linear coordinate change in the angular domain with the parameter relation $d\theta = \theta_s ds = \lambda ds$, for λ a constant. It follows that the energy functional (4.2) converts to a function of the N control points:

$$E(R_1, \ldots, R_N) = \int_0^{N-1} \left(\lambda^{-1} R_s\right)^2 + \left(\lambda^{-2} R_{ss}\right)^2 + (R(s) - R_\tau(s))^2 \lambda ds$$

for the B-spline radius given by:

$$R(\theta(s)) = R(s) = \sum_i c_i(s) R_i, \quad \text{for } s \in [0, N-1] \tag{4.3}$$

Since we seek for the control points R_i, $i = 1, \ldots, N$ that minimize the former energy, they must satisfy the system:

$$\frac{\partial E}{\partial R_j} = 0, \forall i \in \{1, \ldots, N\}$$

The jth equation is:

$$\left(\frac{2}{\lambda^2}\right) \sum_i \left(\int \dot{c}_j \dot{c}_i \right) R_i + \left(\frac{2}{\lambda^4}\right) \sum_i \left(\int \ddot{c}_j \ddot{c}_i \right) R_i + \sum_i \left(\int c_j c_i \right) R_i = \int c_j R_\tau$$

It follows that the system of equations (4.3) can be written in matrix form as:

$$(B_1 + B_2 + B_0)R = BR = F_\tau$$

here the entries of B_j are sums of the jth derivatives of the spline coefficients c_i. The term $(B_1 + B_2)$ corresponds to the stiffness matrix for B-splines snakes and B_0 is the extra term coming from our particular external energy. The forces F_τ induced by the target curve are computed via the parameter change $R_\tau(\theta(s))$, for $\theta(s) = \sum_i c_i(s)\theta_i$.

Since, in our problem, F_τ does not depend on R, the solution is explicitly given by:

$$R = B^{-1} F_\tau$$

The cartesian transform of the polar spline given by the above radial control points is our final adventitia model.

Figure 4.9 shows the whole adventitia closing process. The adventitia mask (fig.4.9(a)) obtained from the classification stage is first closed with ACC (fig.4.9(b)) and finally approached with a B-snake (fig.4.9(c)). the green curve in (fig.4.9(c)) is the final snake one would obtain from the initial snake in red.

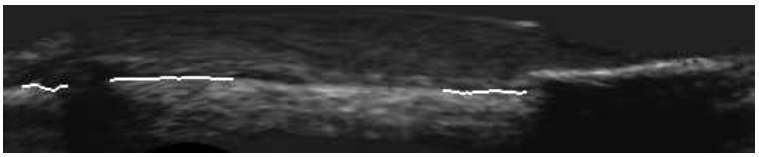

(a)

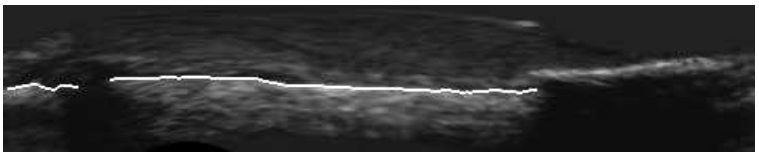

(b)

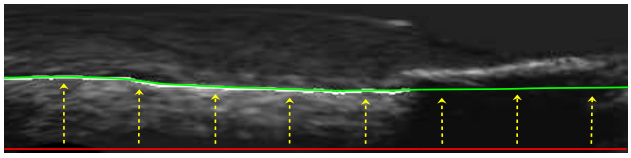

(c)

Figure 4.9: Adventitia Closing: Adventitia mask (a), ACC closing (b) and final snake (c).

Chapter 5

Validation

5.1 Validation Protocol

5.1.1 Study Group

The study group has been designed to assess the ability of the reported algorithm to detect the adventitia border in the presence of different plaques, artifacts and vessel geometries. A total number of 5400 images extracted from 11 different cases have been tested. The sequences analyzed are clinical cases of the Hospital Universitari Germans Trias i Pujol in Badalona (Spain). We have segmented 22 vessel segments of a length ranging from 4 to 6 mm (200-300 frames) and including:

1. 6 segments with uncomplete vessel borders due to side-branches and sensor guide shadows.
2. 5 calcified segments.
3. 9 segments with non calcified plaque.
4. 2 normal segments.

For each segment, the adventitia has been manually traced every 10 frames by 4 experts in IVUS image interpretation, which yields a total number of 540 validated frames with 4 different manual models each.

5.1.2 Accuracy Measures

To assess segmentation accuracy, the automatically detected borders have been compared to the manual models. Accuracy is quantified with the following standard measures:

1. *Absolute and Signed Distances.*

   Distance maps to manual contours serve to compute the difference in position between automatic and manually traced curves. Such maps encode for each pixel, $p = (x_p, y_p)$, its distance to the closest point on the manual contour:

$$\begin{aligned} D(p) &= \min_{q\in\gamma}(d(p,q)) = \\ &= \min_{q\in\gamma}\left(\sqrt{(x_p - x_q)^2 + (y_p - y_q)^2}\right) \end{aligned} \tag{5.1}$$

where q are points on the manually identified contour. Signed distances ($SgnD$) [36] weight the value $D(p)$ depending on wether the pixel p lyes inside or outside the target curve γ. Its mean value detects any bias in curve position, that is, wether detections are systematically bigger or smaller than manual segmentations.

We will consider absolute (in mm) and relative (in %) distance errors. Absolute errors are given by formula (5.1), while relative ones are the ratio:

$$RelD(p) = 100 \cdot \frac{D(p)}{d(q, O)}$$

where the origin, O, is the mass center of the manual contour and q is the point achieving the minimum in (5.1). Since relative errors take into account the true dimensions of the vessel, they reflect positioning errors better.

For each distance error, its maximum and mean values on the automated contour are the error measures used to assess position accuracy. If PixSze denotes the image spatial resolution and p is any point on the automatically traced adventitia, then the set of functions measuring accuracy in positions are:

- **Maximum distance errors** (in mm and %):

$$MaxD = \max_p (D(p) \cdot PixSze)$$
$$RMaxD = \max_p (RelD(p))$$

- **Mean distance errors** (in mm and %):

$$MD = \text{mean}_p (D(p) \cdot PixSze)$$
$$RMD = \text{mean}_p (RelD(p))$$

- **Mean signed distance error** (in mm):

$$MSD = \text{mean}_p (SgnD(p) \cdot PixSze)$$

2. *Area Differences.*

Binary images of manual, $I_M(i, j)$, and automatic, $I_A(i, j)$, borders serve to compute the following measure for area accuracy:

- **Percentage of Area Differences**

$$AD = 100 \cdot \frac{\sum_{i,j} |I_M(i, j) - I_A(i, j)|}{\sum_{i,j} I_M(i, j)}$$

The interval given by the mean $\pm$ standard deviation computed over the 4 experts contours indicate the statistical range of values for each of the automated errors (MaxD, RMaxD, MD, RMD and AD). However, accuracy in models strongly depends on the pixel resolution as well as on the (manual) visual identification of the adventitia layer. These dependencies have two main consequences. The first one hinders any comparison to other segmentation algorithms as the minimum error (in mm) depends on pixel

precision. The second one, implies that an analysis of automated errors might not reflect, by its own, the true accuracy of segmentations, since a large variation range might be caused by a significant difference among experts models. A standard way [45] of overcoming the above phenomena is by comparing automated errors to the variability among different manual segmentations (inter-observer variability). Inter-observer variability is obtained by computing the error measures for the models made by two independent observers and it, thus, quantifies discrepancy among experts. A Student T-test is used to determine if there is any statistical significant difference between inter-observer and automated distance errors.

5.2 Parameters Tunning

Filtering parameters remove spurious fake detections from the discrimination stage. There are two main candidates to act as filtering parameters of the vessel borders masks, length filtering and area filtering. An exhaustive study determine which is the best set of parameters achieving an optimal segmentation of manually traced borders. By collecting all the parameters controlling the segmentation algorithm, we obtain an error function of 4 variables, $E(\tau_{PF1}, \rho_X, \rho_F, \tau_{PF2})$. Although the proper way of setting the parameters achieving an optimal segmentation of manually traced borders would be to find out the global minimum of the former function, for the sake of a reduction in the computational time required in the training stage, we adopt the following strategy. First, we note that the only way to obtain a global minimum of the function E is by an exhaustive search in its parameter space $(\tau_{PF1}, \rho_X, \rho_F, \tau_{PF2})$, as we lack of an analytic expression for the cost error function. On one hand, we have to choose the thresholds for vessel borders mask, $\tau_{PF1}, \rho_X, \rho_F$. For τ_{PF1}, we have to choose it among all thresholds ensuring at least 90% of true C_1 detections, so τ_{PF1} is a sample of thresholds that ensures this percentage of detections. ρ_X is a radial percentile used to compute an image sensitive threshold for discriminating between adventitia points and the rest of the pixels classified by τ_{PF1}, so ρ_X is a sample of percentiles. Finally, we have to decide between an area filtering or a length filtering and choose the number of pixels as area or the percentile as length, so ρ_F divides in ρ_A and ρ_L and they convert in variables. On the other hand, we have to choose the threshold for calcium mask, τ_{PF2} among all thresholds that ensure at most a 10% of noise, so τ_{PF2} is another sample of thresholds. In this way, for every set of values $\tau^j_{PF1}, \rho^j_X, \rho^j_F, \tau^j_{PF2}$, we obtain a value of our error function. It follows that we need the computation of the whole process for every set of frames, increasing the computational cost of our study. For the moment, in this work and after a little study of a few patients, we have heuristically fixed ρ_X at 6% and the samples of τ_{PF1} and τ_{PF2} at 3 different values. We perform the filtering parameter learning by analyzing the mean and maximum absolute segmentation errors for a training set of 12 vessel segments which are representative of all kinds of plaques and vessel morphologies. The different samples are:

$$\begin{aligned} \rho_A &= \{90, 100, 110, 120, 130, 140, 150, 160, 170, 180, 190, 200, 210\} \\ \rho_L &= \{77, 78, 79, 80, 81, 82, 83, 84, 85, 86, 87, 88\} \end{aligned}$$

for each combination (τ_{PF1}, τ_{PF2}) of the thresholding parameters, obtaining a different function of ρ_A as an area filtering and ρ_L as a length filtering. These combinations of thresholding parameters are:

$$\text{Adv0Cal1} = (0.0567, -0.1241) \quad \text{Adv0Cal2} = (0.0567, -0.1468) \quad \text{Adv0Cal3} = (0.0567, -0.1295)$$
$$\text{Adv1Cal1} = (0.0578, -0.1241) \quad \text{Adv1Cal2} = (0.0578, -0.1468) \quad \text{Adv1Cal3} = (0.0578, -0.1295)$$
$$\text{Adv2Cal1} = (0.0619, -0.1241) \quad \text{Adv2Cal2} = (0.0619, -0.1468) \quad \text{Adv2Cal3} = (0.0619, -0.1295)$$

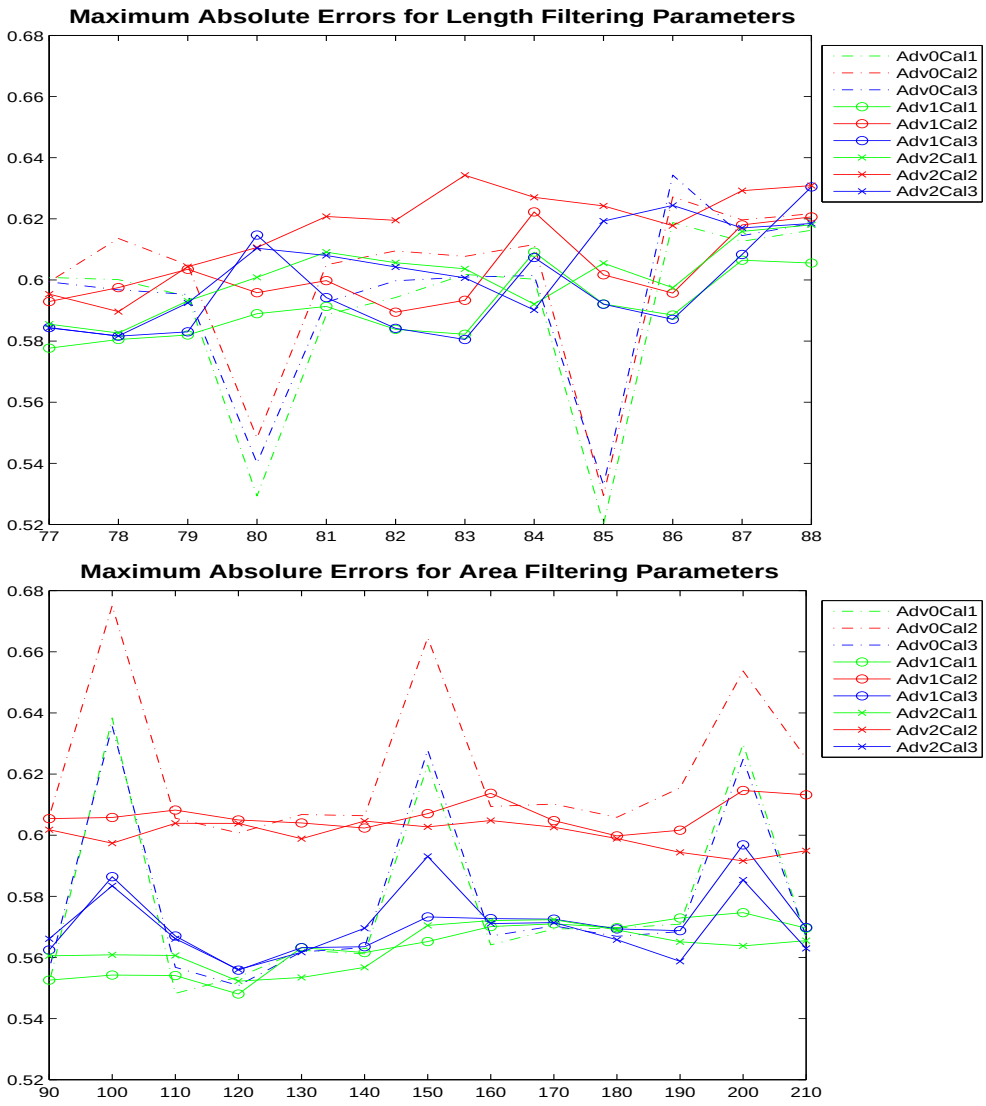

Figure 5.1: Maximum Absolute Error function for Length and Area Filtering Parameters

Figures 5.1 and 5.2 show the different error functions, maximum absolute error functions (fig.5.1) and mean absolute error function (fig.5.2), both for area and length filtering parameters. Each curve corresponds to a combination (τ_{PF1}, τ_{PF2}) with area or lenght filtering parameters as a variable. As we can see, both minimum of error functions correspond to the combination Adv0Cal1 and the length filtering parameter $\rho_L = 85\%$, obtaining the following results.

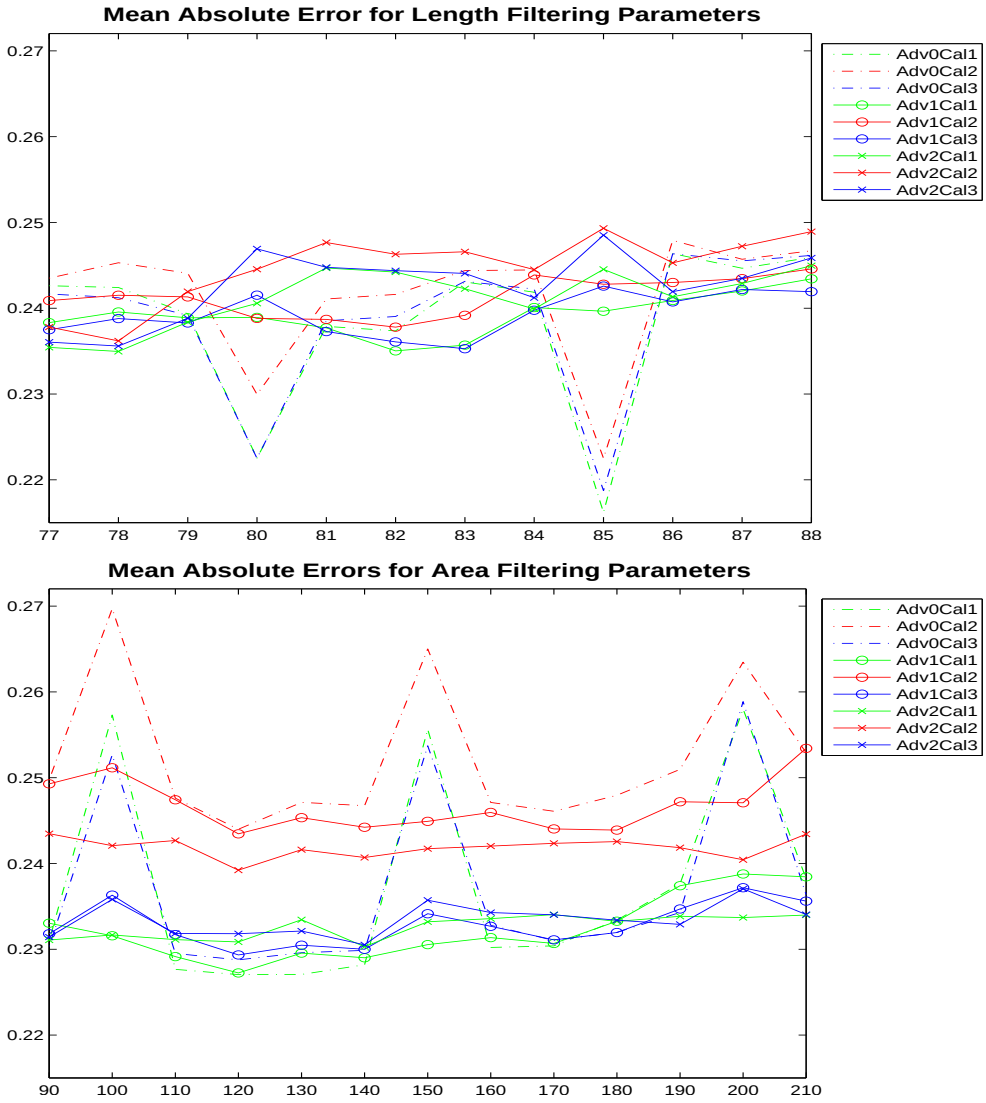

Figure 5.2: Mean Absolute Error function for Length and Area Filtering Parameters

We have validated our strategy in sequences captured with a Boston Scientific Clear View Ultra scanner at 40 MHz with constant pull-back at 0.5 mm/sec and acquisition rate of 25 frames/sec. The digitalized sequences are 384×288 images with a spatial resolution of 0.0435 mm per pixel. The set of optimal parameters for a Boston Clear View is given by:

$$PF1 = 0.1906X + 0.9817Y$$

with thresholding parameters set to:

$$\tau_{PF1} = 0.0567; \rho_X = 6\%; \rho_F = 85\%$$

for computation of vessel borders mask and

$$PF2 = -0.1498PF1 + 0.9887Z, \qquad \tau_{PF2} = -0.1241$$

for the calcium mask. The adventitia detection parameters ensure a 99.95% of true C_1 detections. We note that, by the feature space definition, we only have a 17% of false positives, which just represent 6% of the total number of points classified in C_1. This fact favors the use of a length filtering on adventitia detections as fake response remover. In the case of calcium extraction, the threshold achieves less than a 1% of noise and ensures 90.2156% of calcium detections.

5.3 Real Cases

Some of the adventitia segmentations achieved with the presented strategy are shown in this section and we split them in four different cases: the first (figure 5.3) corresponds to normal vessel segments, the second (figure 5.4) to vessel segments with soft plaque. The third (figure 5.5) have been extracted from calcified vessel segments and finally, the last one (figure 5.6) shows images with missing information, mainly due to side branches and sensor guide shadows.

1. NORMAL SEGMENTS In the first column we present a normal segment, whereas in the second one, the vessel presents non-fibrous plaque.
2. SOFT PLAQUE SEGMENTS In the first column, we present a vessel segment with lipidic plaque, whereas, in the second column, the vessel segment contains soft plaque. Notice that in the anisotropic contour closing step (fig.5.4(l) to fig.5.4(m)) we use image borders continuity, since these images come from cartesian coordinates. Thus, although adventitia points before the ACC do not appear on the right of the image, ACC closes in the two directions from the left side of the image.
3. CALCIFIED PLAQUE SEGMENTS In this case, both vessels contain calcified plaque. Notice that, although intima is detected, both polar coordinates and a rigid snake, yield that the final closed model corresponds to the adventitia.
4. SIDE BRANCHES AND SENSOR SHADOW SEGMENTS Both vessel segments lack of information, the first due to a calcified area plus a side branch and the second column, because of sensor shadow and a little side branch. The key point of this kind of images is the sparse information, which we discuss in chapter 7.

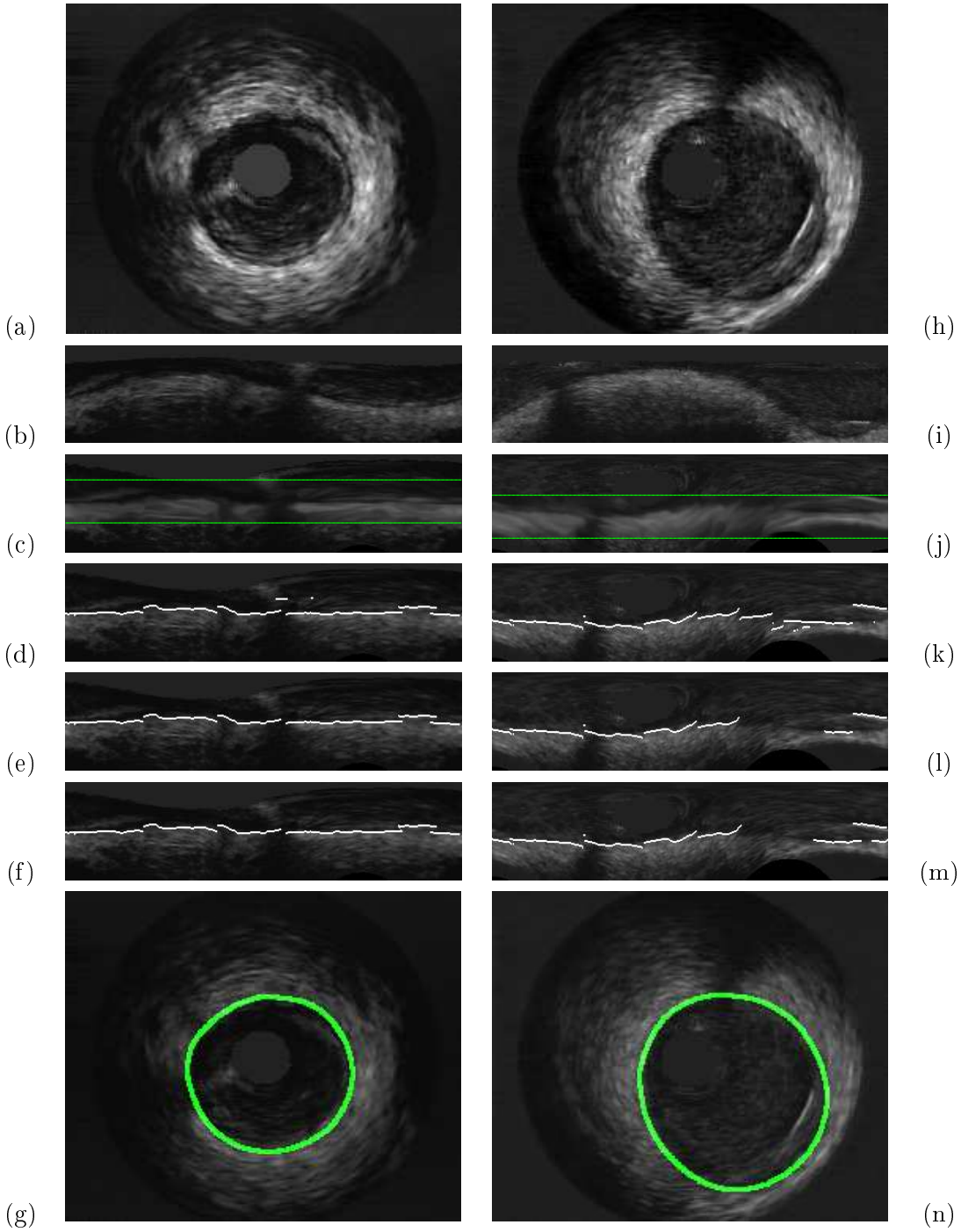

Figure 5.3: Automated Adventitia Detections for Normal Vessel Segments

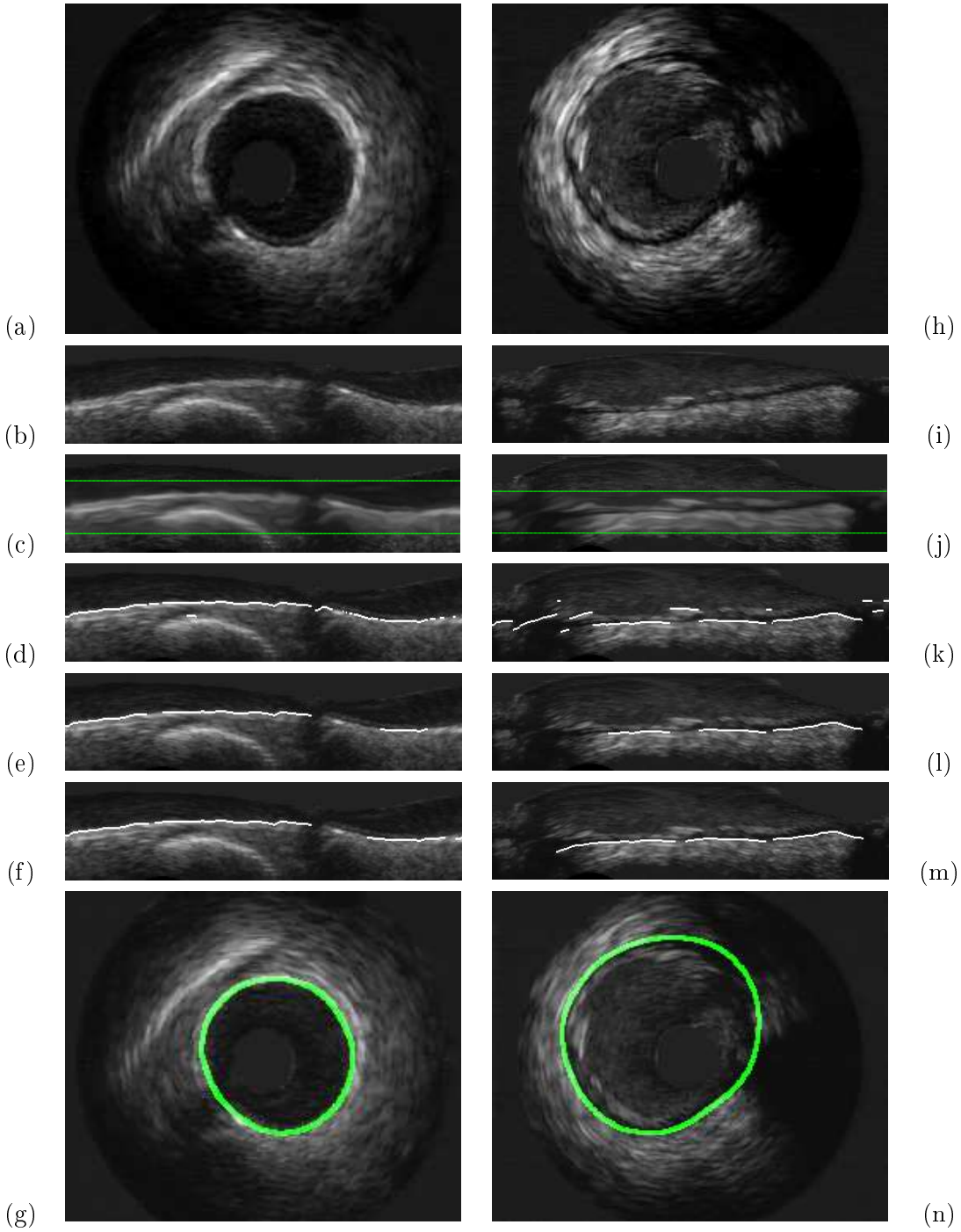

Figure 5.4: Automated Adventitia Detections for Vessel Segments with Soft Plaque

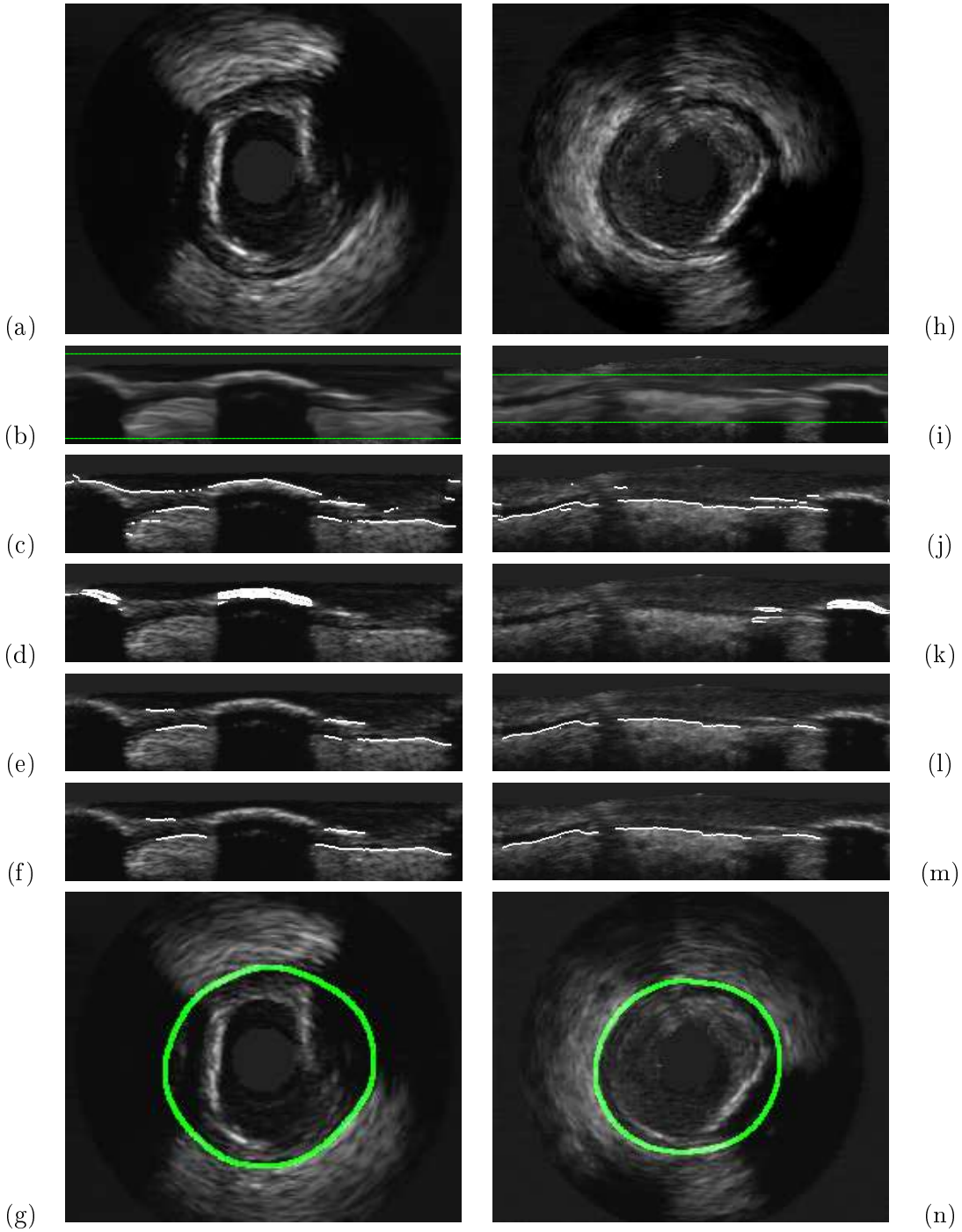

Figure 5.5: Automated Adventitia Detections for Calcified Vessel Segments

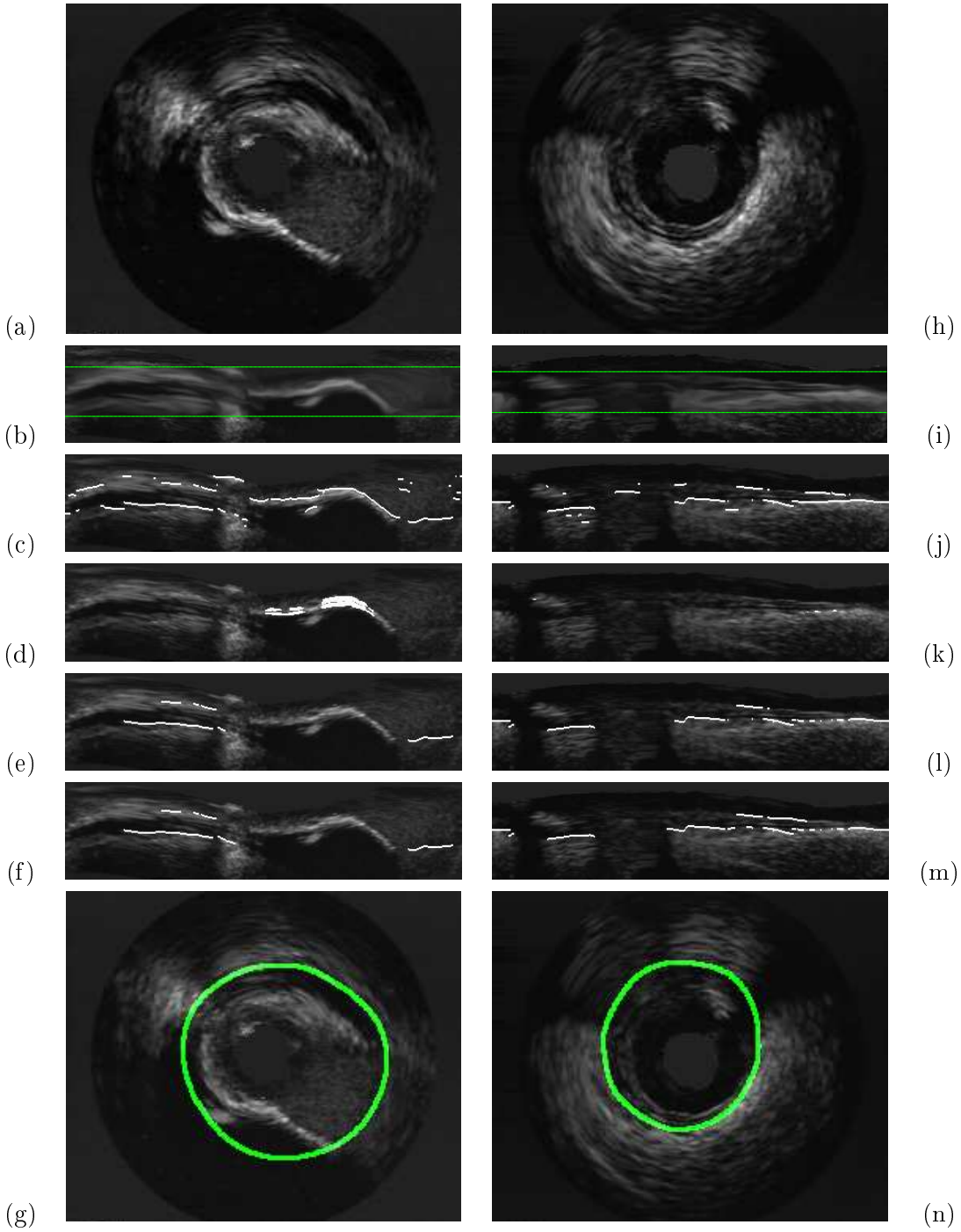

Figure 5.6: Automated Adventitia Detections for Uncomplete Vessel Segments

5.3.1 Statistics

In this section we give our statistical analysis of the segmentation errors. We have analyzed errors individually for each patient gathered by vessel plaque nature and globally. Whisker boxes are usual to analyze within patient variability and confident intervals serve to detect any significant difference between different plaques.

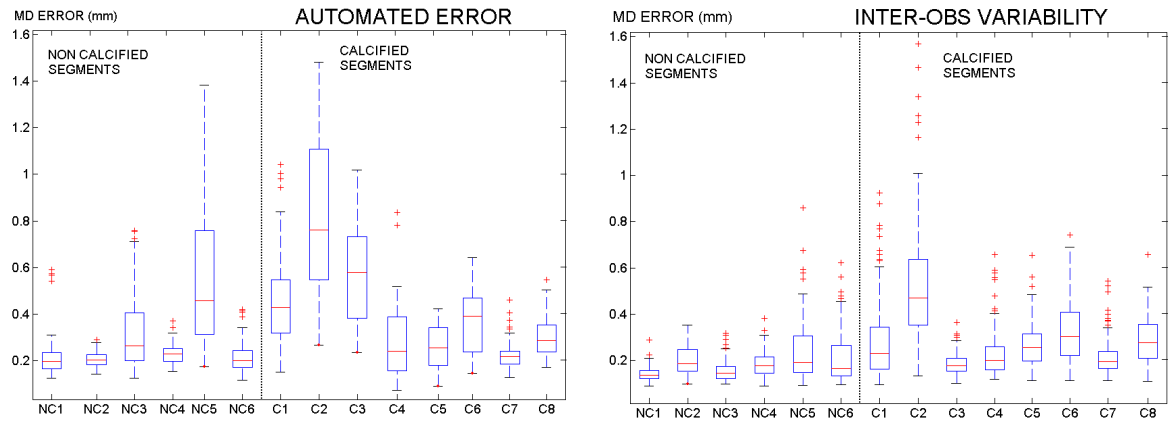

Figure 5.7: Whisker Boxes for Automated Error,(a), and Inter-Observer Variability, (b).

Figure 5.7 shows whisker boxes for mean distance absolute errors (fig.5.7(a)) and mean inter-observer variations (fig.5.7(b)) for soft plaque and calcium segments. Each box contains the mean distance errors obtained from the 4 experts segmentations (80 to 120 samples per box) for a single vessel segment. Boxes labelled with **NC** correspond to non-calcified segments and those labelled with **C** to calcified ones. An analysis of the whisker boxes reflects robustness of segmentations: the smaller the boxes are, the more reliable the method is. Whisker boxes serve to visually detect any anomaly in the models. In general terms, the means of automated errors are slightly higher than inter-observer variability means. However, since automatic segmentations present a significantly smaller variation range than inter-observer variability, our segmentations are within the experts discrepancy rate (see T-tests comparing means summarized in table5.3. Lack of reliable information at large angular sectors, significantly increases errors variability in calcified segments,both for manual segmentations and automatic detections. The large range of the whisker box of the case C2 detects it as a vessel segment of difficult manual identification that should be excluded from any statistical analysis. Larger boxes for automated detections (fig.5.7(a)) in cases NC5 and C3 comparing to their counterparts in fig.5.7(b) indicate that there are specially difficult cases for our segmenting strategy. We devote the discussion section 7.1 to a detailed analysis of such miss detections.

Statistical ranges (mean $\pm$ standard deviation) for automatic errors (AUT) and inter-observer variability (INT-OBS) are summarized in tables 5.1 and 5.2. Patients presenting an unusual large inter-observer variability have been excluded, since we consider they are anomalous cases with difficult and non robust manual identification. We present statistics for non-calcified segments in the first column of 5.1, calcified ones in the second column of the same table and a total population of 20 vessel segments in table 5.2.

Table 5.1: Performance Evaluation of the Adventitia Segmentation Strategy. Automatic Errors versus Inter-Observer Variability for non-calcified and calcified segments

	NON-CALCIFIED		CALCIFIED	
	INT-OBS	AUT	INT-OBS	AUT
MaxD (mm)	0.4208 ± 0.1794	0.4238 ± 0.1026	0.6627 ± 0.3610	0.7161 ± 0.2532
RelMaxD (%)	0.3963 ± 0.1788	0.3868 ± 0.1075	0.5469 ± 0.3171	0.6116 ± 0.2665
MeanD (mm)	0.1783 ± 0.0698	0.1864 ± 0.0364	0.2650 ± 0.1306	0.2885 ± 0.0947
RelMeanD (%)	0.1647 ± 0.0668	0.1684 ± 0.0387	0.2142 ± 0.1113	0.2388 ± 0.0931
Area Dif. (%)	6.6799 ± 3.1579	7.2571 ± 1.9842	9.3511 ± 5.7529	10.0428 ± 4.0390
SgnMeanD (mm)	0.0004 ± 0.0769	0.0283 ± 0.0540	0.0163 ± 0.1213	-0.0381 ± 0.0912

Table 5.2: Performance Evaluation of the Adventitia Segmentation Strategy. Automatic Errors versus Inter-Observer Variability for all segments

	TOTAL	
	INT-OBS	AUT
MaxD (mm)	0.5386 ± 0.3075	0.5715 ± 0.2296
RelMaxD (%)	0.4697 ± 0.2664	0.5122 ± 0.2344
MeanD (mm)	**0.2206 ± 0.1126**	**0.2265 ± 0.0688**
RelMeanD (%)	0.1888 ± 0.0945	0.1972 ± 0.0662
Area Dif. (%)	**7.9813 ± 4.7962**	**8.6032 ± 3.3436**
SgnMeanD (mm)	0.0081 ± 0.1013	**0.0041 ± 0.0801**

A summary of the results of the T-tests comparing the inter-observer variability and automatic errors averages is given in table 5.3. We report the p-value and the confidence interval for the difference in means. Statistics exclude outliers and T-tests are computed over the total errors in table 5.2.

Table 5.3: Statistics Summary on T-tests comparing the means of Inter-Observer Variability and Automatic Errors.

	Confidence Interval (CI)	p-value
MeanD	(-0.002684,0.014491)	0.177721
Area Dif.	(-0.017985,0.114350)	0.153404
SgnMeanD	(-0.002401,0.010787)	0.212219

According to a two tailed T-test, there is no significant difference between inter-observer and automated mean absolute distance errors and difference in areas. For mean distance errors the p-value equals $p = 0.177721$ and the confidence interval for the true difference in means at a significance level of 95% is $CI = (-0.002684, 0.014491)$. In the case of percentage in area difference, $p = 0.153404$ and the interval (also at a significance level of 95%) is $CI = (-0.017985, 0.114350)$. Maximum errors for automated detections are slightly above the range of maximum inter-observer variability. In order to robustly de-

termine the fraction of increase, we use a single tailed T-test to check if the null hypothesis statement "the mean of automated maximum errors is above λ times the mean of maximum inter-observer variabilities" is true. The true proportion between maximum automated error and inter-observer variability is between the minimum λ rejecting the null hypothesis and the maximum accepting it. For $\lambda = 1.102$, the null hypothesis was accepted with a p-value, $p = 0.053901$ and for $\lambda = 1.103$, it was rejected with $p = 0.049846$. We conclude that the increase in maximum automated errors is under a 10.3%. Finally a T-test on the mean of the automated signed distance error shows that in average it is zero as the p-value equals $p = 0.212219$ and the confidence interval for the true mean is a tiny interval containing the zero value $CI = (-0.002401, 0.010787)$.

Chapter 6

Application

In order to make this strategy feasible for the experts as well as to validate more patients and achieve a systematic analysis of the main source of errors in clinical cases, we have developed a prototype of application in Matlab. The application allows the analysis of a vessel segment by means of a simple interface to facilitate its use by physicians. The steps to get a sequence segmented are summarized in the following figures.

The expert has to choose, from "New Segmentation" the desired patient of a list.

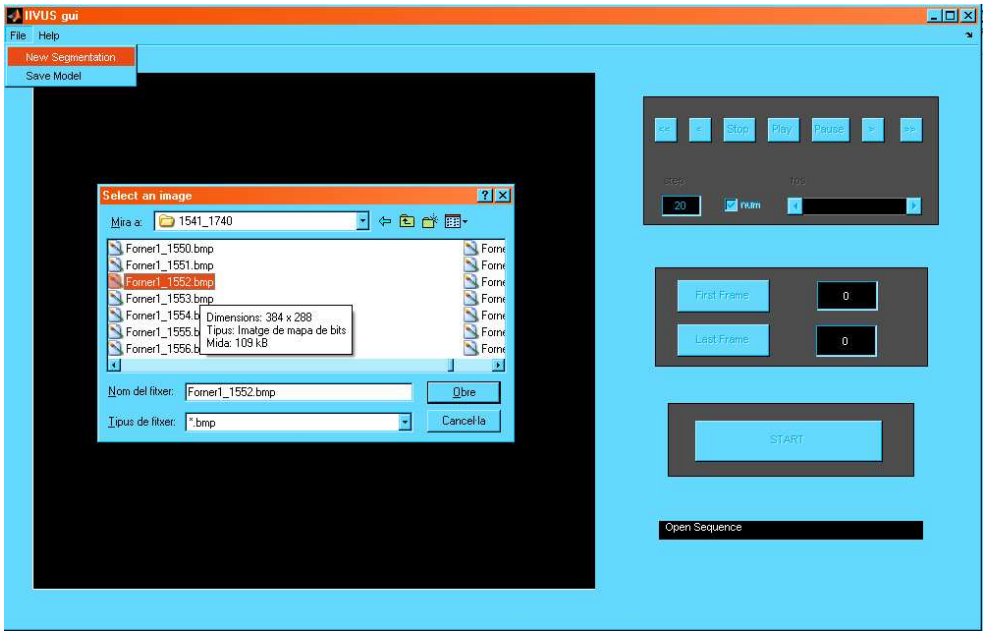

Figure 6.1: First step of the application

Then, the whole sequence is loaded and the expert can view all the sequence, or can pass the sequence frame by frame or every a number of frames determined in the "step" box.

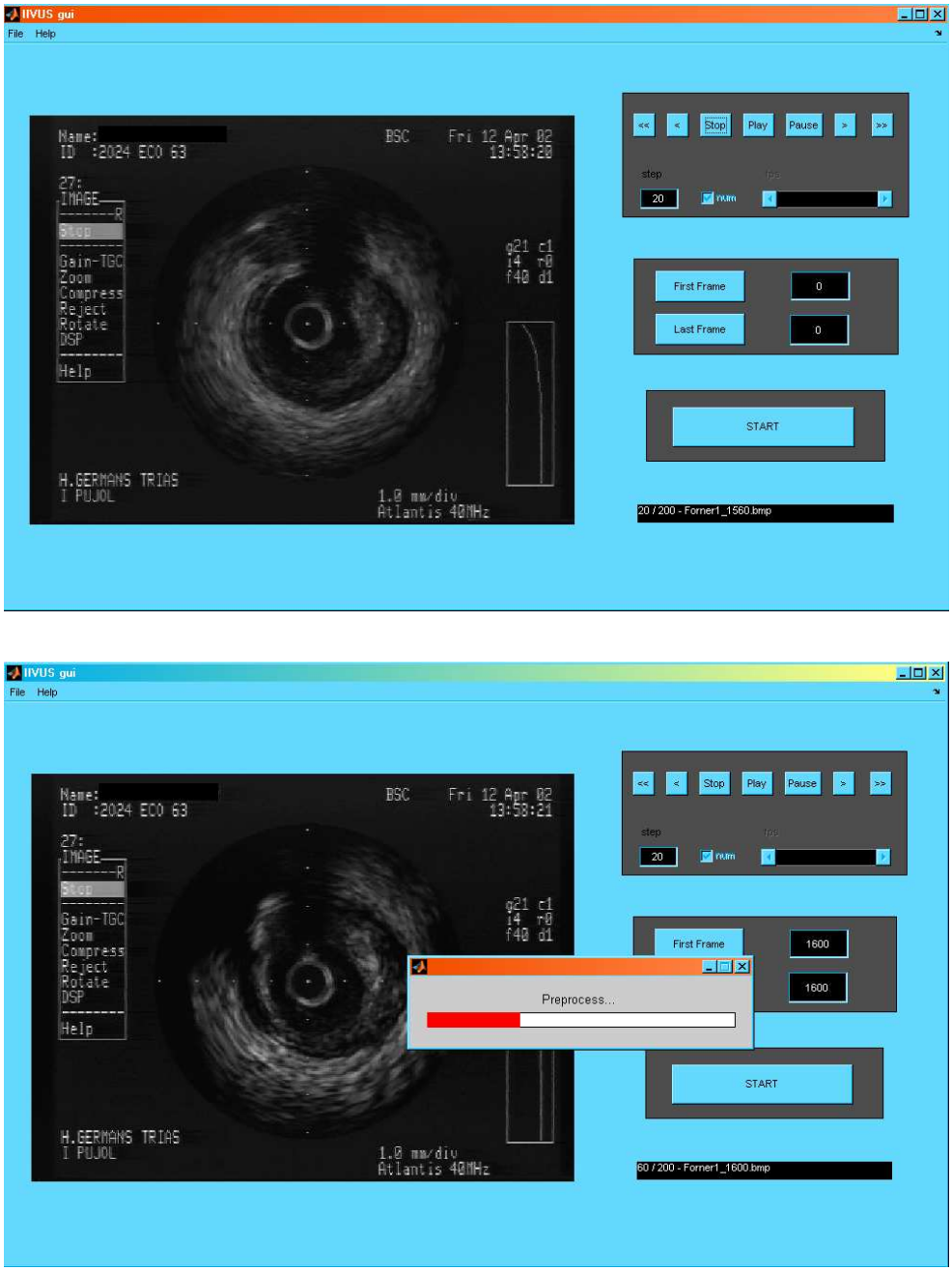

Figure 6.2: The starting of the process

The expert decides the first and the last frame to segment and the automatic process starts.

The screen shows the results of the different steps and finally, the final result.

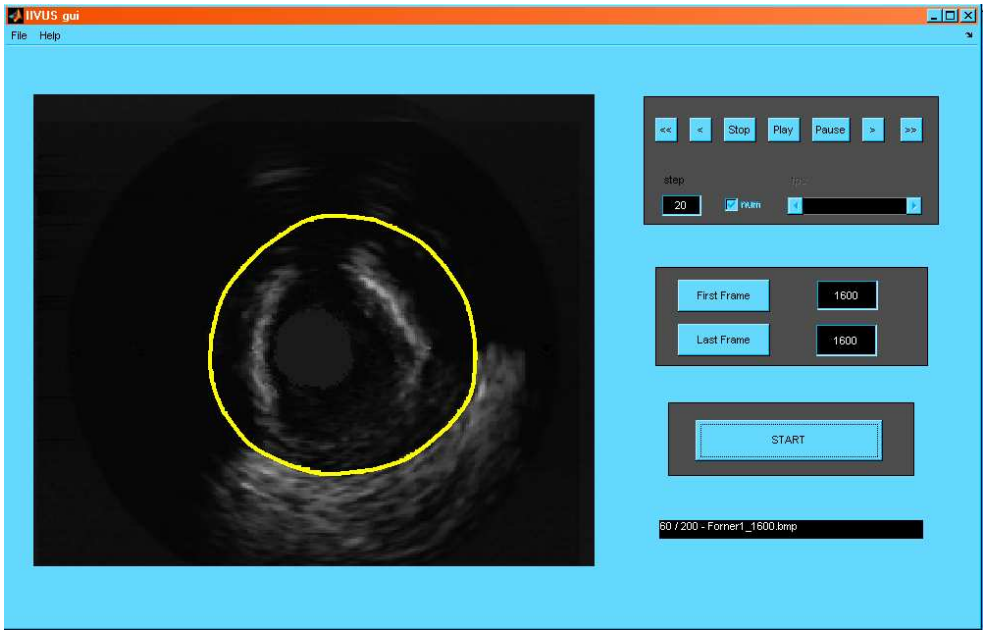

Figure 6.3: Final Result

Chapter 7

Discussion and conclusions

7.1 Discussion

The combination of a priori knowledge (classification techniques) with filtering techniques based on continuity of image geometry is the key point for a robust characterization of vessel (the adventitia layer, in our case) borders. By designing an accurate point selection strategy, we avoid human interaction and the use of longitudinal cuts and ECG-gated acquisitions. The latter results in a save in the computational time required for the automatic segmentation. On a pentium IV at 3.2 Ghz and 1G of RAM, the implementation in MatLab 7.0 takes approximately 35 minutes to model 200 frames.

The reliability of the proposed strategy is reflected in the global statistics extracted from in vivo sequences segmentation. The fact that, both, mean distances and vessel areas compare to inter-observer variation validates our method for extraction of clinical measurements. Since there is no bias in automated segmentations (the mean signed distance is statistically zero) we can ensure that our method achieves an optimal compromise among experts criteria. That is, with the exception of the isolated frames that deviated maximum errors from inter-observer range, automatically traced curves lie between curves traced by different observers. The number of outlier bad segmentations requiring manual correction represent less than a 15% of the studied valid cases and, with the computing tools available, the time spend in their manual correction is in the range accepted by clinical experts.

Still, the striking increase in the error range for the anomalous cases NC5 and C3 needs to be analyzed. Such miss detections correspond to vessel segments that either the adventitia is hardly identified or there is severe lack of valid information.

Weak visual appearance of the adventitia border is a technical limitation of the UltraSound acquisition technique and it is cause of disagreement among experts (case NC2 in fig.5.7(b)) in 9% of the cases. Our strategy suffers this kind of error in 18% of the segments under study (boxes NC5, C2 and C3 in fig.5.7(a)). We argue that the only way to minimize the impact of border blurring is taking into account tissue motion periodicity along the sequence. Even for physicians it is difficult to identify vessel borders by an analysis of still images. Often, they use cardiac periodicity in the movement of vessel structures to distinguish between tissue and other structures. We are currently assessing if adding Fourier analysis of image grey level statistics to the set of adventitia descriptors reduces the number of this type of wrong detections.

The second source of large error in automatic detections is lack of information. Calcium sectors or side branches can take up large angular sectors, thus, distorting information at these sectors. In

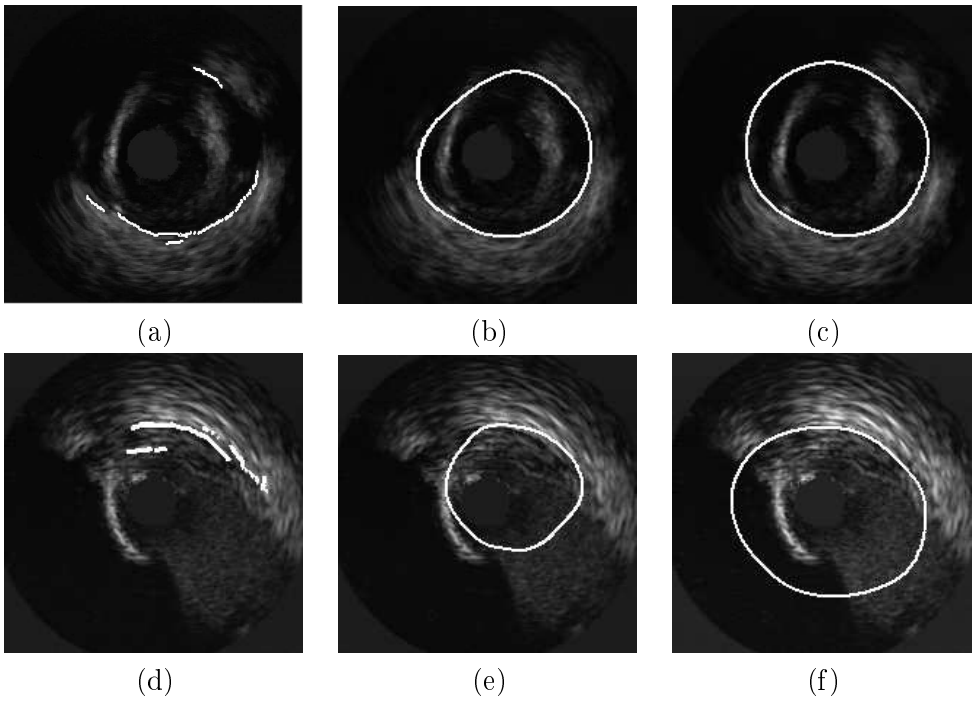

Figure 7.1: Adventitia models in images with sparse information. Points detected (a), (d), final snake (b), (e) and manual model (c), (f).

the case that the sparse valid information is not uniformly distributed along angular sectors, the final elliptic model is prone to underestimate the border true radial position. Fig.7.1 illustrates the scarce bad distributed information artifact. On the first column we show an image with uniformly enough point distribution and on the second column a pathological case with all available information gathered in the first quadrant of the image. Images in fig.7.1(a), (d) depict the ACC closure modelled by the B-snake in fig.7.1(b), (e). The true manually traced contours are shown in fig.7.1(c), (f).

Lack of strong 3D continuity in the B-snake closing of candidate points on the vessel borders is the main source of the above error. The use of 2D NURBS (spline surfaces) instead of 1D splines could reduce the impact of missing information. However, in our case, they might not succeed in correcting this kind of miss interpolations. On one hand, NURBS can only take into account local deformations and continuity of the surface. On the other hand, the previously described pathology is prone to happen at large vessel segments. It follows that NURBS interpolation might imply handling the segmentation of the whole image sequence block (over 1200 frames). Such large amount of data is computationally unfeasible (we recall that, at most, we handle 300 frames). One possible way of overcoming lack of information for large vessel segments would be mimicking the experts strategy used for manually tracing the adventitia borders. Our application [27] to manually segment vessel borders shows the previous border on the current image to be segmented and allows the physician to modify it. An informal survey on the key points and frames used by the expert for border tracing at images with severe lack of information prompts that they usually keep the model traced on the last valid frame. This suggests using the information available at the last frame with adventitia points detected in more than 70% of the vessel angular sectors to complete vessel borders at images with sparse detections.

7.2 Conclusions

Vessel border detection is of especial interest for plaque assessment and quantification of lumen narrowing in IVUS sequences. By its weak appearance, there are few algorithms addressing segmentation of the external adventitial border. In this work we propose a general strategy for vessel border detection in IVUS images with an explicit application to the segmentation of the medial-adventitial border.

The reported methodology combines classification techniques with advance smoothing operators based on image level sets continuity. The strategy for media-adventitia detection is a three-step algorithm. We show that using geometric knowledge of image structures suffices to detect the adventitia without precise and exhaustive classification of vessel tissue. Besides our segmenting strategy is robust against a large variety of vessel cases, such as presence of different plaques, side-branches, IVUS artifacts (echo shadowing, sensor guide) and lost of information.

The strategy has been tested on 5400 images including calcified and non calcified vessel segments, side-branches and the most representative shadowing artifacts of intravascular ultrasound sequences. The comparison to borders manually traced by 4 experts shows that in 84% of the cases we are within the range of inter-observer variability, which demonstrates the optimality of the automated model. An exhaustive analysis of those cases increasing the error rate determines that the main source of error are bad image acquisition and more than 75% of missing information due to calcium shadowing.

7.3 Future work

There are two main vias to improve this procedure: improving the accuracy of segmentations and working in a systematic setting of the optimal segmenting parameters in order to turn our strategy into a generic modelling algorithm for any acquisition device.

For the first via, two lines of research (currently in progress) are suggested to minimize the scope of erroneous detections. Taking into account periodicity in tissue movement in the point selection stage and mimicking the experts strategy for border interpolation at segments of significant lack of reliable information.

For the second via, as we explained in section 5.2, we obtained a 4 variables function of error and we fixed three parameters. In spite of the good results, only studying the filtering parameters, in a segmentation problem, all the parameters play a role, and they are all involved in the solution of the problem. Thus, we will make an exhaustive study of the dependency of the error function respect to all the critical parameters. To ensure that the minimum found out is not an outlier, we will find a minimum neighborhood .

Another point is to prove more accurately the robustness of the method by computing the intra-observer variability (the amount of variation one observer experiences when observing the same material more than once) and "intra-sequence" variability (the amount of variation one sample of the sequence is made comparing with another sample of the same sequence taking into account the cardia motion).

A more further research will be the embedding of this strategy with the strategy described in [46] to the intima segmentation and tissue characterization to develop an application for the automatic segmentation of the vessel borders and tissue characterization. Once the experts have proven its efficiency, we will work on the 3D reconstruction of the vessel border, by means of IVUS images.

Bibliography

[1] D. Hausmann, A.J.S. Lundkvist, G. Friedrich, K. Sudhir, P.J. Fitzgerald and P.G. Yock, " Lumen and Plaque Shape in Atherosclerotic Coronary Arteries Assessed by In Vivo Intracoronary Ultrasound Beyond Angiography". *XX Congres of the ESC*, vol. 1, 1998.

[2] GS Mintz, SE Niessen, WD Anderson, SR Bailey, R erbel, PJ Fitzgerald, FJ Pinto, K Rosenfield, RJ Siegel, EM Tuzcu, PG Yock, "ACC Clinical Expert Consensus Document on Standards for the acquisition measurement and reporting of intravascular ultrasound studies: a report of the American College of Cardiology Task Force on Clinical Expert Consensus Documents (Commitee to Develop a Clinical Expert Consensus Documents on Standrads for Acquisition, Measurement and Reporting of Intravascular Ultrasound Studies [IVUS])", *J Am Coll Cardiol*, vol. 37, pp. 1478:1492, 2001.

[3] GS Mintz, AD Pichard, KM Kent, LF Satler, JJ Popma,MB Leon, "Axial plaque redistribution as a mechanism of percutaneous transluminal coronary angioplasty". *Am J Cardiol* vol. 77(5),pp. 427:430, 1996.

[4] J. Dijkstra, G. Koning, J.C. Tuinenburg, P.V. Oemrawsingh, J.H.G. Reiber, "Automatic Border Detection in IntraVascular UltraSound Images for Quantitative Measurements of the Vessel, Lumen and Stent Parameters", *Computer Assisted Radiology and Surgery - CARS 2001*, International Congress Series 1230, pp. 916:922.

[5] C. von Birgelen, C. D. Mario, W. Li, J. C. Schuurbiers, C. J. Slager, P. J. de Feyter, J. R. Roelandt, and P. W. Serruys, "Morphometric analysis in three-dimensional intracoronary ultrasound: An in vitro and in vivo study performed with a novel system for the contour detection of lumen and plaque", *Amer. Heart J.*, vol. 132, pp. 516:527, 1996.

[6] C. von Birgelen, G. S. Mintz, A. Nicosia, D. P. Foley, W. J. van der Giessen, N. Bruining, S. G. Airiian, J. R. T. C. Roelandt, P. J. de Feyter, and P. W. Serruys, "Electrocardiogram-gated intravascular ultrasound image acquisition after coronary stent deployment facilitates on-line three-dimensional reconstruction and automated lumen quantification", *J. Amer. Coll. Cardiol.*, vol. 30, pp. 436:443, 1997.

[7] M. Sonka, X. Zhang, S. C. DeJong, S. M. Collins, and C. R. McKay, "Automated detection of coronary wall and plaque borders in ECG-gated intravascular ultrasound pullback sequences (abstract)", *Circulation*, vol. 94, pp. 1:653, 1996.

[8] P.A. Brathwaite, K.B. Chandran, D.D. McPherson, E.L. Dove, " Lumen detection in human IVUS images using region-growing", *Computers in Cardiology 1996*, pp. 37:40.

[9] D. Gil, P. Radeva, J. Saludes, "Segmentation of artery wall in coronary IVUS images: a probabilistic approach", *Proceedings of the International Conference on Pattern Recognition (ICPR'00)*, vol.4, pp. 352–355, 2000.

[10] P.A. Brathwaite, K.B. Chandran, D.D., McPherson, "3D IVUS border detection in highly diseased arteries with dissecting flaps", *Computers in Cardiology 1998* pp. 157–160, 1998.

[11] Z. Luo, Y. Wang, W. Wang, "Estimating Coronary Artery Lumen Area With Optimization-Based Contour Detection", *IEEE Trans. On Med. Imag.*, vol. 22, no. 4, 2003.

[12] E. Brusseau, C.L. de Korte, F. Mastik, J. Schaar, Anton F. W. van der Steen, "Fully Automatic Luminal Contour Segmentation in Intracoronary Ultrasound Imaging: A Statistical Approach", IEEE Trans. Med. Imag., vol. 23, no. 5, 2004.

[13] M. Sonka and X. Zhang and M. Siebes et al. "Segmentation of intravascular ultrasound images: A knowledge based approach", IEEE Trans. on Medical Imaging.14: 719:732. 1995.

[14] M.E. Olszewski, A. Wahle, S.C. Mitchell, M. Sonka, "Segmentation of intravascular ultrasound images: a machine learning approach mimicking human vision", *CARS 2004*, pp. 1045:1049.

[15] X. Zhang, M. Sonka, "Tissue characterization in intravascular ultrasound images", *IEEE Trans. on Medical Imaging*, vol. 17, no.6, pp. 889:899, 1998.

[16] O. Pujol, P. Radeva, "Supervised Texture classification for Intravascular Tissue Characterization", in *Handbook of Medical Image Analysis: Advanced Segmentation and Registration Models*, Kluwer Academic/Plenum Pub. (2004).

[17] C. Haas, H. Ermert, S. Holt, P. Grewe, A. Machraoui, J. Barmeyer, "Segmentation of 3D intravascular ultrasonic images based on a random field model", *Ultrasound Med. Biol.*, vol. 26, no. 2, pp. 297:306, 2000.

[18] A. Takagi, K. Hibi, X. Zhang, T. J. Teo, H. N. Bonneau, P. G. Yock, P. J. Fitzgerald, "Automated contour detection for high-frequency IVUS imaging: a technique with blood noise reduction for edge enhancement", *Ultrasound Med. Biol.*, vol. 26, no. 6, pp. 1033:1041, 2000.

[19] M.E. Plissiti, D.I. Fotiadis, L.K. Michalis, G.E. Bozios, "An Automated Method for Lumen and Media-Adventitia Border Detection in a Sequence of IVUS Frames", *IEEE Trans. on Information Tech. in Biomedicine*, vol. 8, no. 2, pp. 131:141, 2004.

[20] JD. Klingensmith, R. Shekhar, DG. Vince, "Evaluation of three-dimensional segmentation algorithms for the identification of luminal and Medial-adventitial borders in intravascular ultrasound", *IEEE Trans. on Med. Imag.*, vol. 19, no.10, pp. 996:1011, 2000.

[21] J. Dijkstra, G. Koning and J.H.C. Reiber, "Quantitative measurements in IVUS images". *The International Journal of Cardiovascular Imaging.* vol. 15, no 6, pp. 513:522, 1999.

[22] A. Hernandez, D. Gil, P. Radeva, E. Nofrerias, "Anisotropic Processing of Image Structures for Adventitia Detection in IVUS Images", *IEEE Proc. CiC 2004*, vol. 31, pp. 229:232.

[23] K. Fukunaga, "Introduction to Statistical Pattern Recognition", 2nd Ed.,*Academic Press*, New York, 1990.

[24] W.F. Young, S. McLaughlin, "Pseudo-inverse filtering of IVUS images", *Science, Measurement and Technology*, IEE Proceedings- vol. 145, Issue 6, pp. 321:326, 1998.

[25] M. Rosales, P. Radeva, "Simulation Model of Intravascular Ultrasound Images", *Medical Image Computing and Computer - Assisted Intervention , MICCAI 2004*, LNCS (3217),pp. 200:207, 2004.

[26] X.M. Pardo, P. Radeva, D. Cabello, "Discrimant snakes for 3D reconstruction of anatomical organs", *Medical Image Analysis*, vol. 7, pp. 293:310, 2003.

[27] O. Rodriguez, D. Rotger, J. Mauri, E. Fernandez, V. Valle, P. Radeva, "Active vessel workstation: three-dimensional reconstruction of coronary arteries by fusion of angiography and intravascular ultrasound", *European Society of Cardiology Congress*, Munich, 2004.

[28] F. Vilariño, P. Radeva, "Cardiac Segmentation with Discriminant Active Contours", *Artificial Intelligence Research and Development*. IOS Press, pp:211:215, 2003.

[29] M. Kass, A. Witkin and D. Terzopoulos, "Snakes: Active Contour Models", *Int. Journal of Computer Vision*, vol. 1(4), pp. 321:331, 1987.

[30] M. Brejl, M. Sonka, "Object localization and border detection criteria design in edge-based image segmentation: automated learning from examples", *IEEE Trans. on Medical Imaging*, vol. 19 (10), October 2000.

[31] T. F. Cootes, A. Hill, C. J. Taylor, and J. Haslam, "Use of active shape models for locating structures in medical images", *Image Vision Comput.*, vol. 12, pp. 355:365, 1994.

[32] D. Gil, A. Hernàndez, J. Mauri, P. Radeva, "A Deterministic-Statistic Strategy for Media-Adventitia Border Modelling in IVUS Sequences", *IEEE Transactions on Medical Imaging*, (under second revision).

[33] D. Gil, "Geometric Differential Operators for Shape Modelling", *PhD Tesis, Universitat Autonoma de Barcelona*, 2004 (available at http://www.cvc.uab.es/ debora/)

[34] D. Gil, P. Radeva, "Extending Anisotropic Operators to Recover Smooth Shapes", *Comp. Vis. Imag. Unders.*, (to appear)

[35] R. Duda, P. Hart, "Pattern Classification", *Wiley-Interscience*, 2001.

[36] V. Caselles, R. Kimmel, G. Sapiro, "Geodesic Active Contours", *Int. Journal of Computer Vision*, vol. 22, no.1, pp. 61:79, 1997.

[37] D.R. Martin, C.C. Fowlkes, J. Malik, "Learning to detect natural image boundaries using local brightness, color and texture cues", *IEEE PAMI*, vol. 26, pp. 1:20, 2004.

[38] C. Van Rijsbergen, *Information Retrieval*, second ed. Dept. of Computer Science, Univ. of Glasgow, 1979.

[39] R. Carmona, S. Zhong, "Adaptative smoothing respecting feature directions", *IEEE Trans. Image Proc.*, vol. 7, no. 3, 1998.

[40] P. Perona, J. Malik, "Scale space and edge detection using anisotropic diffusion", *Proc. IEEE Comp. Soc. Workshop on Comp. Vision, IEEE Computer Society Press*, pp. 16-22, 1987.

[41] J. Weickert, "A Review of Nonlinear Diffusion Filtering, Scale-Space Theory in Computer Vision", *Lecture Notes in Comp. Science*, Springer-Verlag, 1997.

[42] A. López, D. Lloret, J. Serrat, "Creaseness measures for CT and MR image registration", *CVPR'98*, 1998.

[43] L.C. Evans, "Partial Differential Equations", *Berkeley Math. Lect. Notes*, 1993.

[44] B. Jähne, "Spatio-temporal image processing". *Lecture Notes in Comp. Science*, vol. 751, Springer, 1993.

[45] J.R. Landis, G.G. Koch, "The measurement of observer agreement for categorical data", *Biometrics*, vol. 33, pp.159:74, 1977.

[46] O. Pujol, "A Semi-Supervised Statistical Framework and Generative Snakes for IVUS Analysis", *PhD Tesis, Universitat Autonoma de Barcelona*, 2004.